THE PHOTOMETRIC AND KINEMATIC STRUCTURE OF FACE-ON DISK GALAXIES. I. SAMPLE DEFINITION, Hα INTEGRAL FIELD SPECTROSCOPY, AND H I LINE WIDTHS

David R. Andersen[1,2]

NRC Herzberg Institute of Astrophysics, 5071 West Saanich Road, Victoria, BC V9E 2E7, Canada; david.andersen@cnrc-nrc.gc.ca

Matthew A. Bershady, Linda S. Sparke, John S. Gallagher III, and Eric M. Wilcots

Department of Astronomy, University of Wisconsin, 475 North Charter Street, Madison, WI 53706;
mab@astro.wisc.edu, sparke@astro.wisc.edu, jsg@astro.wisc.edu, ewilcots@astro.wisc.edu

Wim van Driel

Observatoire de Paris, Section de Meudon, GEPI, CNRS UMR 8111; and Université de Paris 7, 5 Place Jules Janssen,
92195 Meudon Cedex, France; wim.vandriel@obspm.fr

and

Delphine Monnier-Ragaigne

Laboratoire de l'Accélérateur Linéaire, Université Paris-Sud Orsay, 91898 Orsay Cedex, France; monnier@lal.in2p3.fr

ABSTRACT

We present a survey of the photometric and kinematic properties of 39 nearby, nearly face-on disk galaxies. Our approach exploits echelle-resolution integral-field spectroscopy of the Hα regions, obtained with DensePak on the WIYN 3.5 m telescope Bench Spectrograph. These data are complemented by H I line profiles observed with the Nançay radio telescope for 25 of these sample galaxies. Twelve additional line widths are available for sample galaxies from the literature. In this paper, we introduce the goals of this survey, define the sample selection algorithm, and amass the integral field spectroscopic data and H I line widths. We establish spatially integrated Hα line widths for the sample. We test the veracity of these spatially integrated line profiles by convolving narrowband imaging data with velocity field information for one of the sample galaxies, PGC 38268, and also by comparing to H I line profiles. We find H I and Hα line profiles to be similar in width but different in shape, indicating that we are observing different spatial distributions of ionized and neutral gas in largely axisymmetric systems with flat outer rotation curves. We also find vertical velocity dispersions of the ionized disk gas within several disk scale lengths have a median value of 18 km s^{-1} and an 80% range of 12–26 km s^{-1}. This is only a factor of ∼2 larger than what is observed for neutral atomic and molecular gas. With standard assumptions for intrinsic and thermal broadening for Hα, this translates into a factor of 3 range in turbulent velocities, between 8 and 25 km s^{-1}.

Subject headings: galaxies: kinematics and dynamics — galaxies: spiral — galaxies: structure

Online material: machine-readable table

1. INTRODUCTION

Two fundamental and intertwined cosmological questions are how galaxies form and come to have their present structure. The current approach to answering these questions involves comparing numerical and semianalytical structure-formation models to a suite of critical observations of low- and high-redshift galaxies (e.g., Navarro et al. 1996, 1997; van den Bosch 2000). For nearby disk galaxies one of the salient observations that tests and constrains structure-formation models is a measurement of halo shape.

An increasing number of cosmological simulations show that dark matter halos are naturally triaxial (Davis et al. 1985; Frenk et al. 1988; Dubinski & Carlberg 1991; Jing et al. 1995; Jing & Suto 2002), but other physical processes, such as the dissipative infall of gas during formation, may transform the halo into an oblate spheroid (Dubinski 1994). If dark matter halos are nonspherical, then this should have an observational impact on the luminous matter in disks. Theory predicts a number of observational consequences including effects on (1) the orbits in lopsided galaxies (Levine & Sparke 1999; Jog 1999, 2002; Noordermeer et al. 2001); (2) the formation and structure of bars and oval distortions (Athanassoula 2004); and (3) noncircular motions in dark matter dominated low surface brightness (LSB) galaxies (Hayashi et al. 2004). Triaxial halos also should beget elliptical disks (Franx & de Zeeuw 1992; Jog 2000). Because disk asymmetries may be linked to the shape of the halo, it is interesting to measure deviations from axisymmetry. Indeed, many galaxies appear to have lopsided light distributions (e.g., Zaritsky & Rix 1997; Kornreich et al. 1998; Conselice et al. 2000; Bournaud et al. 2005), H I distributions (e.g., Baldwin et al. 1980), integrated H I line profiles (Richter & Sancisi 1994), or kinematic features (e.g., Richter & Sancisi 1994; Swaters et al. 1999; Kornreich et al. 2000, Chemin et al. 2006), especially in LSB galaxies (Swaters et al. 2003; Simon et al. 2003). However, a direct measurement of disk ellipticity is challenging because it is difficult to disentangle the intrinsic shape of galaxy disks from both projection effects and spiral structure (e.g., Rix & Zaritsky 1995; Schoenmakers et al. 1997; Schoenmakers 1999; Andersen et al. 2001; Barnes & Sellwood 2003). If better estimates of ellipticity existed, tighter limits could be placed on halo triaxiality.

This paper describes our disk structure survey. With this survey, we attempt to constrain the halo shapes of field galaxies by

[1] Max-Planck-Institute for Astronomy, Königstuhl 17, D-69117 Heidelberg, Germany.
[2] Visiting Astronomer, Kitt Peak National Observatory. KPNO is operated by AURA, Inc., under contract to the National Science Foundation.

measuring disk lopsidedness and ellipticity using a combination of bidimensional spectroscopy and imaging, complementing other work such as the Fabry-Perot kinematic survey of Virgo cluster disk galaxies (Chemin et al. 2006). Beyond the implications such asymmetry measurements have for cosmological simulations of galaxy halos, both quantities also should be sources of scatter in the TF scaling relation (Franx & de Zeeuw 1992; Zaritsky & Rix 1997; Andersen & Bershady 2003). Therefore, a measurement of ellipticity, and possibly lopsidedness, places limits on other astrophysical sources of TF scatter, including disk mass-to-light ratios. If limits are placed on the variation of disk mass-to-light ratios, a new constraint will be placed on mass decomposition models.

In this paper we present the Hα and H I kinematic data for our survey. Hα echelle observations were made with the integral field unit (IFU) DensePak (Barden et al. 1998) on the WIYN 3.5 m telescope[3] for 39 nearly face-on disk galaxies. H I observations for 23 of the sample come from the Nançay radio telescope. The optical data forms the primary kinematic data for this survey. The purpose of the H I line profiles is to establish that the optical integral-field data amply samples the potential. While H I and Hα have similar flux-weighted radial extents in many cases (Verheijen & Sancisi 2001), there will still exist different and varying spatial distributions and "turbulent" motions of ionized and neutral gas, which could lead to significant differences between H I and Hα integrated line widths. However, our expectations are that turbulent motions are small; the differences between ionized and neutral turbulent motions smaller still; and the differences in spatial distribution are mitigated by the typically flat, and steeply rising rotation curves of this sample. Verifying these expectations is important for our ultimate goal of measuring halo shapes and also allows us to address the suitability of optical line widths as dynamical tracers of total mass. The application has relevance to studies of both nearby and distant galaxies. The combination of optical and radio data also is pertinent to understanding the origin of line profile asymmetries.

In future papers in this series we analyze the Hα and H I line profiles, the Hα velocity fields, and the photometric properties of the survey galaxies. These studies explore the photometric and kinematic asymmetries of the galaxy sample, and their correlations. The studies build a physical picture of why asymmetries arise, how they contribute to scatter in the Tully-Fisher relation, and how well total dynamical mass can be measured in nearly face-on systems. Together, they allow us to study the ellipticity distribution of our sample in a tertiary analysis.

The present paper is organized as follows. We provide the selection algorithm in § 2. We present the DensePak and Nançay observations in § 3. The basic processing of the data is detailed in § 4. H I line widths are also presented in § 4. In § 5 we describe how we combine integral-field observations to obtain Hα integrated line widths, present measurements of turbulent motions, discuss integrated line profiles of individual galaxies, and contrast optical and radio line profiles. We conclude with a summary in § 6.

2. SELECTION ALGORITHM

The selection of the sample for this survey is driven by our desire to measure disk ellipticity. A 10% disk ellipticity will create differences in observable quantities that are smaller than typical measurement errors for inclined galaxies (Barnes & Sellwood 2003; Andersen et al. 2001), thereby necessitating that our sample
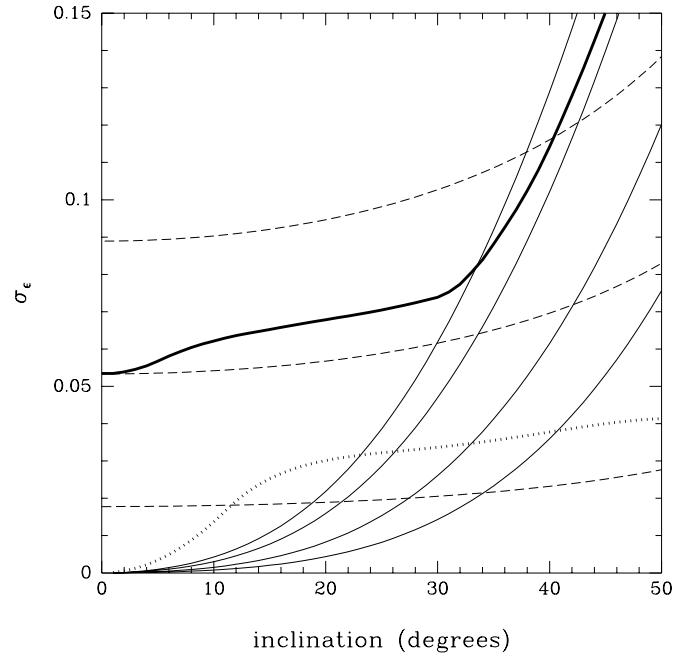
Fig. 1.—Confidence limit (68%) error distribution in intrinsic disk ellipticity, σ_ϵ, vs. inclination. The lighter solid lines represent the contribution to the ellipticity error due to the measurement errors of $5°$, $7°$, $10°$, and $12°$ in the difference between kinematic and photometric position angles (σ_ψ). The dashed lines are the contribution to the error on ellipticity due to 0.01, 0.03 and 0.05 axis ratio measurement errors ($\sigma_{b/a}$). The dotted line is the ellipticity error due to kinematic inclination errors (σ_i). For each inclination angle, we used an empirical relationship between inclination and kinematic inclination to estimate the error (Andersen & Bershady 2003). The heavy solid line is the total ellipticity error as a function of inclination for the inclination error, $\sigma_\psi = 10°$ and $\sigma_{b/a} = 0.03$. Ellipticity errors were calculated assuming an ellipticity of 0.1 and that the intrinsic ellipticity major axis is aligned with the kinematic major axis. While the details of these curves vary slightly for different ellipticities and phase angles between the ellipticity and kinematic axes, it is always true that ellipticity errors increase with inclination.

include only nearly face-on galaxies. To illustrate this, Figure 1 shows how measurement errors on observable quantities translate into intrinsic ellipticity errors as a function of inclination. We have assumed that intrinsic ellipticity is measured via a comparison of observed photometric and kinematic position angles, photometric axis ratios, and kinematic inclinations. A description of the method is found in Andersen et al. (2001). Given the expected errors on these quantities and that the mean intrinsic ellipticity of galaxies is expected to be below 10%, galaxies with inclinations <30° are optimum choices for intrinsic ellipticity measurements.

Two methods exist for making a selection of nearly face-on disks: Galaxies can be chosen with photometric axis ratios close to unity, or chosen with narrow H I line widths (or other kinematic measures of rotation). The Tully-Fisher relationship can be inverted; line widths and absolute magnitudes can be used to solve for inclination (Rix & Zaritsky 1995). Because the scatter in the Tully-Fisher relation is small for normal spirals, these so-called "inverse Tully-Fisher" inclinations could be used to select galaxies with inclinations less than 30°.

Choosing galaxies with existing H I line widths may bias a sample. Many galaxies are selected for H I observations on the basis of having photometric inclinations greater than 45° for inclusion in Tully-Fisher studies. Those galaxies with narrow H I line widths may indeed be nearly face-on, but in this case they are necessarily highly elliptic. Hence, surveys built on the availability of H I line widths as a selection criterion may preferentially include spiral galaxies with elliptical disks. We therefore choose galaxies for this study based on photometric axis ratios.
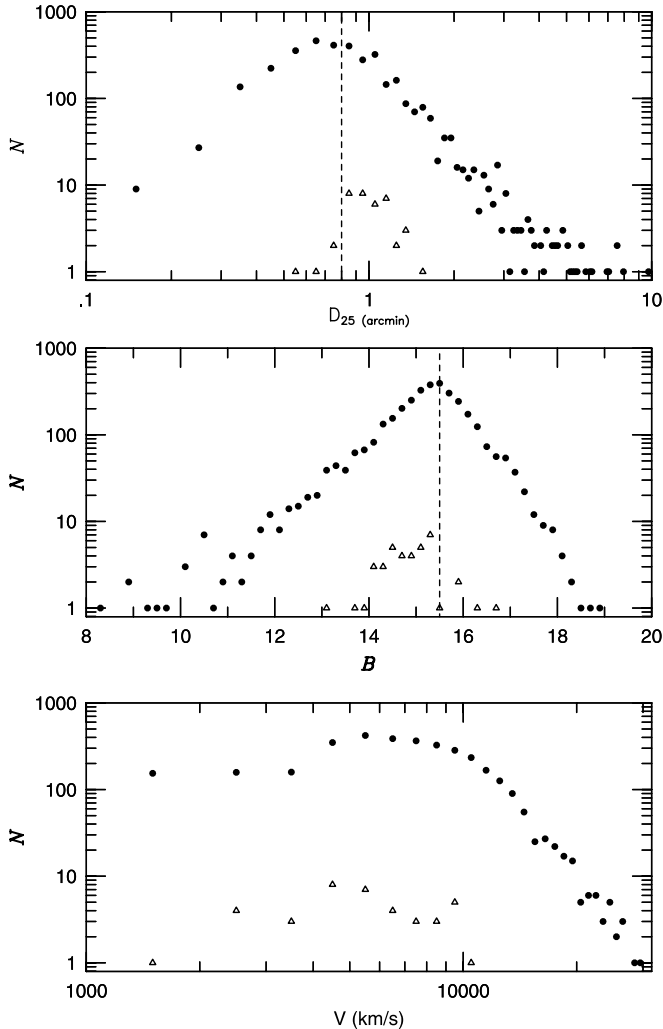
FIG. 2.—Distribution of diameters (D_{25}; *top panel*), blue magnitudes (B; *middle panel*) and recession velocities (V; *bottom panel*) for galaxies in the PGC meeting the selection criteria in § 2 (*filled circles*) and galaxies observed as part of this survey (*open triangles*). Specifically, these selection criteria include (1) $1.5 < t\text{-type} < 8.5$, (2) $A_B < 0.6$, (3) $\delta_{1950} > -10°$, and (4) $b/a_{25} + \Delta b/a_{25} > 0.87$. Completeness criteria for galaxies in the PGC are met for $D_{25} > 0.'8$ and $B < 15.5$. Despite the incompleteness of the parent sample, we endeavored to choose a representative sample of disk galaxies that spanned a wide range in types and luminosities.

However, disks with the greatest ellipticities will appear nearly face-on only if the intrinsic minor axis lies near the inclination axis. This potential bias is a second-order effect that can be accounted for when modeling the distribution in ellipticities for the general population of spiral galaxies (Ryden 2004). We therefore chose galaxies with axis ratios near unity.

The DensePak integral field unit on the WIYN telescope spans $30'' \times 45''$, so targets were limited to diameters (D_{25}) between $45''$ and $75''$ so they could be well sampled in a few pointings. Given this relatively small size, chosen galaxies will typically be some of the faintest and most distant galaxies in the catalogs of nearby galaxies.

To maximize the number of galaxies available for study, we chose our sample from the LEDA database[4] which contains all galaxies in common catalogs (e.g., NGC, UGC, IC), plus additional galaxies only defined in the Principal Galaxy Catalog (PGC; Paturel et al. 1997). While the PGC is inclusive of many

[4] See http://leda.univ-lyon1.fr.

other galaxy catalogs, galaxies with diameters less than $\sim 1'$ still fall below the completeness threshold (Fig. 2). We required sample galaxies from LEDA to have (1) axis ratio $b/a + \Delta b/a > 0.87$ ($i - \Delta i < 30°$),[5] (2) apparent disk size $45'' < D_{25} < 75''$, (3) Galactic absorption $A_B < 0.6$ (Schlegel et al. 1998), (4) declinations visible from WIYN, $\delta_{1950} > -10°$, (5) observed B-band magnitudes, (6) observed recession velocities, and (7) t-types ranging from Sab to Sd (t-types between 1.5–8.5). We elected not to observe Sa galaxies because these galaxies have less Hα emission than later types (Kennicutt et al. 1989). Of the 1300 targets that met these raw selection criteria, 753 were observable during our longest WIYN DensePak runs (1999 January and December; $0^h < \text{R.A.} < 13^h$).

We obtained Second Generation Digitized Sky Survey (DSS2) images to further refine our sample selection. After visual inspection, we eliminated from our sample galaxies with bars, rings, interacting companions, or foreground stars that contaminated the inner isophotes. This step removed 60% of the sample from consideration. We measured scale lengths, position angles, and axis ratios from the DSS2 images using the IRAF `ellipse` routine, and we further required (1) a relatively constant position angle in the outer portions of the disk, therein removing most warped galaxies, and (2) our measurements of $b/a > 0.87$ on DSS2 images at 3 scale lengths. Between $0^h < \text{R.A.} < 13^h$ only 70 targets remained. As a test of the completeness of our selection criteria, we examined the DSS2 images of every PGC galaxy in a 1 hr slice of right ascension and ascertained that our selection criteria successfully yielded every galaxy with a photometric inclination less than $30°$ in this slice of right ascension. Through the course of our observations, we observed 32 of these 70 targets, plus 7 other galaxies chosen from the same parent sample of 1300 targets, but which lie between $13^h < \text{R.A.} < 24^h$. The 39 observed galaxies are not representative of the parent sample; rather, we attempted to span a large range of morphological types and luminosity (Table 1 and Fig. 3).

3. KINEMATIC DATA

3.1. *DensePak* Hα *Observations*

We observed 39 sample galaxies with DensePak during 11 nights on 6 separate observing runs (Table 2). The DensePak IFU is a fiber optic array mounted at the Nasmyth f/6.3 focus imaging port on the WIYN 3.5 m telescope. The WIYN Observatory, located on Kitt Peak south of Tucson, Arizona, stands 6875 feet above sea level and is home to the second largest telescope on the mountain. Dedicated in 1994 October, the WIYN telescope employs an altitude-azimuth mount design. DensePak is an array of 91 fibers arranged in a 7×13 fiber rectangle subtending an area of $28'' \times 42''$. Fibers have an active core diameter of $2.''81$ (300 μm). Cladding and buffer increase the total fiber diameter to $3.''75$ (400 μm). According to the DensePak manual's astrometric diagram (Sawyer 1997, Fig. 3)[6] the fiber spacing is $4.''2$ (center-to-center). In addition to the 91 fibers arranged in a

[5] Here $\Delta b/a$ is the uncertainty in the measured axial ratio b/a, and Δi is the corresponding uncertainty in inclination as tabulated in LEDA.

[6] This manual is currently available at http://www.noao.edu/wiyn/densepak .pdf. The astrometric diagram was subsequently published in Homeier & Gallagher (1999). Note there is some uncertainty in the adopted fiber spacing. The plate scale of $10''$ mm^{-1} quote in the manual is incorrect, and should be $9.''374$ mm^{-1} for the bare RC focus of the WIYN port where DensePak was used (see, for example: http://www.noao.edu/wiyn/wiynfacts.html). This reconciles the different fiber diameters quoted here vs. the manual and Homeier & Gallagher. However, it is unclear if the manual's astrometric diagram is based on this erroneous plate scale. For the purpose of this work we adopt the implied fiber spacing given by the numbers in the astrometric diagram.

TABLE 1
Properties of Survey Galaxies Tabulated from the PGC

PGC	Alternate Name	R.A. (B1950)	Decl. (B1950)	Type[a]	t-Type[b]	D_{25}[c] (arcsec)	b/a_{25}[d]	m_B (mag)	A_B[e] (mag)	$V_{\rm helio}$ (km s^{-1})	M_B[f] (mag)
2162..................	UGC 358	00 33 39.0	+01 26 13	Sab	1.8	0.8	0.90	15.5	0.08	5448	−18.9
3512..................	IC 1607	00 56 15.0	+00 19 04	Sb	3.0	0.9	0.87	14.4	0.14	5435	−20.0
5345..................	UGC 1014	01 23 47.1	+06 01 04	SBm	9.2	1.1	0.80	15.2	0.14	2132	−17.3
5673..................	UGC 1087	01 28 46.5	+14 01 13	Sc	5.3	1.2	0.93	14.8	0.23	4485	−19.3
6855..................	UGC 1322	01 48 49.1	+12 53 04	Sc	5.2	1.1	0.81	15.8	0.36	4834	−18.7
7826..................	UGC 1546	02 00 35.1	+18 23 22	Sc	5.4	0.9	0.92	15.2	0.32	2371	−17.6
8941..................	UGC 1808	02 18 16.0	+23 22 20	Sb	3.1	0.9	0.92	14.9	0.39	9447	−21.0
14564..................	NGC 1517	04 06 29.2	+08 31 04	Sc	6.0	1.0	0.85	14.2	1.10	3483	−20.2
15531..................	UGC 3091	04 31 21.2	+01 00 36	Scd	6.7	1.1	0.85	15.1	0.36	5557	−19.6
16274..................	MCG 1-13-8	04 51 19.3	+03 30 46	Sb	2.7	0.8	1.00	15.0	0.32	8915	−20.6
19767..................	UGC 3569	06 48 12.6	+57 13 23	Sd	7.6	0.9	0.83	16.3	0.22	5133	−18.2
20938..................	UGC 3833	07 21 33.4	+32 54 12	Sbc	4.3	0.5	0.88	15.9	0.22	4695	−18.3
23333..................	IC 2283	08 16 16.2	+24 57 00	Sb	3.3	0.9	0.86	14.6	0.14	4654	−19.5
23598..................	UGC 4380	08 20 40.7	+55 00 58	Sc	5.9	0.9	0.95	15.3	0.26	7485	−20.0
23913..................	UGC 4445	08 27 17.2	+61 09 50	Sc	5.3	1.1	0.97	15.3	0.30	6330	−19.7
24788..................	UGC 4614	08 46 06.2	+36 18 20	SBb	2.9	0.7	0.83	15.1	0.15	7556	−20.2
26140..................	NGC 2794	09 13 14.0	+17 47 54	SBbc	4.4	1.1	0.83	14.0	0.14	8760	−21.6
26517..................	UGC 4978	09 19 29.5	+04 06 39	Scd	6.6	1.5	0.84	15.2	0.20	4135	−18.7
27792..................	UGC 5187	09 39 59.1	+41 19 19	SBbc	4.3	0.9	0.81	14.7	0.08	1465	−17.1
28310..................	UGC 5274	09 47 27.1	+16 31 12	SBc	5.9	1.1	0.99	14.7	0.18	5908	−19.9
28401..................	UGC 5277	09 47 46.8	+65 43 32	SBbc	3.6	1.3	0.90	14.4	0.71	3365	−19.7
31159..................	IC 616	10 30 06.6	+16 07 06	Sc	5.9	1.0	0.85	14.8	0.17	5779	−19.9
32091..................	MCG −2-28-6	10 42 40.9	−09 48 04	Scd	6.9	1.3	0.92	14.2	0.15	2511	−18.4
32638..................	NGC 3438	10 49 48.6	+10 48 45	Sbc	3.8	0.8	0.93	14.1	0.10	6488	−20.7
33465..................	UGC 6135	11 01 46.7	+45 23 41	Sbc	3.7	0.9	0.95	13.1	0.03	5948	−21.5
36925..................	NGC 3890	11 46 33.4	+74 34 49	Sc	4.8	0.8	0.92	14.4	0.26	6827	−20.7
38268..................	UGC 7072	12 02 39.6	+29 03 37	Sd	8.0	1.2	0.85	15.3	0.08	3152	−18.0
38908..................	UGC 7208	12 09 56.8	+39 23 20	Sbc	4.4	1.0	0.91	15.0	0.13	7078	−20.1
39728..................	NGC 4275	12 17 21.8	+27 53 54	Sb	2.8	0.8	0.90	14.0	0.09	2317	−18.6
46767..................	NGC 5123	13 20 58.7	+43 20 50	Sc	5.9	1.1	0.89	13.7	0.06	8323	−21.6
49906..................	NGC 5405	13 58 40.3	+07 56 35	Sc	4.8	0.8	0.94	14.9	0.17	6922	−20.0
55750..................	IC 132	15 37 53.7	+20 50 28	Sc	5.4	1.0	0.92	14.5	0.27	4525	−19.8
56010..................	MCG 6-35-5	15 44 37.1	+33 22 38	SBc	6.2	0.8	0.96	15.3	0.14	4468	−18.8
57931..................	UGC 10357	16 20 18.3	+40 33 50	Sbc	3.5	0.8	0.88	15.1	0.05	9280	−20.5
58410..................	UGC 10436	16 29 24.2	+41 15 44	SBc	5.3	1.0	0.97	14.5	0.05	9059	−21.0
70962..................	Mrk 318	23 15 05.9	+13 43 38	Sbc	3.8	0.7	0.80	14.2	0.20	4455	−20.0
71106..................	NGC 7620	23 17 37.3	+23 56 49	Sc	5.9	1.0	0.96	13.8	0.34	9582	−22.1
72144..................	UGC 12740	23 39 22.1	+23 32 15	Sc	6.0	0.6	0.95	16.6	0.27	10521	−19.4
72453..................	UGC 12784	23 45 32.0	+17 11 49	SBbc	3.6	1.3	1.00	14.7	0.30	9952	−21.2

Note.—Paturel et al. (1997). Units of right ascension are hours, minutes, and seconds, and units of declination are degrees, arcminutes, and arcseconds.

[a] de Vaucouleurs type for the galaxy (de Vaucouleurs et al. 1991).

[b] Morphological type placed in a pseudonumerical scale (Paturel et al. 1997).

[c] Diameter measured from the isophote at a B-band surface brightness of $\mu_B = 25$ mag arcsec^{-2}.

[d] Axis ratio measured from the isophote at a B-band surface brightness of $\mu_B = 25$ mag arcsec^{-2}.

[e] A_B is calculated using the galactic absorption law of Cardelli et al. (1989).

[f] Absolute B-band magnitude adopts $H_0 = 75$ km s^{-1} Mpc^{-1} and heliocentric recession velocity corrected for peculiar motion associated with the local group and Virgo cluster.

rectangle, another 4 fibers are spaced around the rectangle roughly an arcminute from the center and are used to measure the "sky" flux. Of the original 91 DensePak fibers, 86 fibers remain—5 fibers are broken (Fig. 4).

DensePak feeds the WIYN Bench Spectrograph, a fiber-fed spectrograph designed to provide low to medium resolution spectra. We used the Bench Spectrograph camera (BSC) and 316 lines mm^{-1} echelle grating in order 8 to cover 6500 Å < $\lambda\lambda$ < 6900 Å, with a dispersion of 0.195 Å pixel^{-1} (8.6 km s^{-1} pixel^{-1}) and an instrumental FWHM of 0.51 Å (22.5 km s^{-1}). We required the highest resolution available with this instrument; fitting velocity field models to galaxies with observed rotation velocities of less than 100 km s^{-1} required centroids with accuracies of roughly 5 km s^{-1}. The BSC images the spectrograph

onto a T2KC thinned SITe 2048 × 2048 CCD with 24 μm pixels. The spectra are aligned along the columns of the CCD. The chip has a read noise of 4.3 e^- and was used with the standard gain of 1.7 e^- ADU^{-1}. The system throughput for this setup is roughly 4% estimated from comparing our mean spectral continuum fluxes to calibrated R-band images (Bershady et al. 2005).

Since galaxy rotation curves typically peak at roughly 2 scale lengths (Persic et al. 1996; Courteau & Rix 1999; Willick 1999) and Hα emission is only detected out to 3–4 scale lengths (Rubin et al. 1999; Dale et al. 2001), our goal was to spatially cover galaxies out to 2.5–3.5 scale lengths. Galaxies with DSS2 scale lengths less than 6″ only required one DensePak position to cover several scale lengths. However, to improve fits to the velocity field we required that two spatial resolution elements
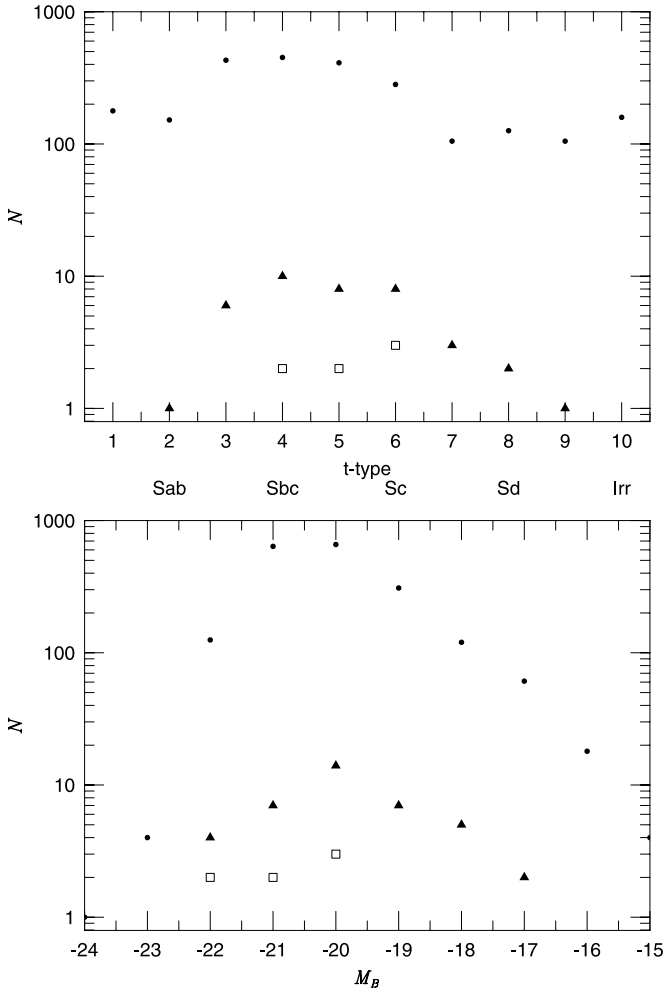
Fig. 3.—Distribution in type (*top panel*) and luminosity (*bottom panel*) for galaxies in the PGC meeting the selection criteria in § 2 (*filled circles*) and galaxies observed as part of this study (*filled triangles*). The selection criteria applied to sample of galaxies in the top panel include, (1) measured B-magnitudes, (2) recession velocities, (3) $A_B < 0.6$, (4) $\delta_{1950} > -10°$, (5) $b/a_{25} + \Delta b/a_{25} > 0.87$, and (6) $0\rlap{.}'6 < D_{25} < 2'$. The bottom panel include all galaxies in the top panel, which have $1.5 < t\text{-type} < 8.5$. We broadened the sample by both type and luminosity on completion of our pilot study (*open squares*; Andersen et al. 2001).

TABLE 2
DensePak Observing Log

PGC	Run ID[a]	UT Date	Exposure Time (s)	Pointings
02162........	e	1999 Dec 22	3600, 3600	2
03512........	e	1999 Dec 21	3600, 2400	2
05345........	e	1999 Dec 20	3600, 3600	2
05673........	f	2000 Dec 29	3600, 3600, 3000	3
06855........	f	2000 Dec 30	3000, 3000, 3000	3
07826........	e	1999 Dec 22	3600, 3600	2
08941........	b	1999 Jan 23	3600, 3600	2
14564........	b	1999 Jan 22	3600, 1800	2
15531........	b	1999 Jan 23	3600, 3600, 3600	3
16274........	e	1999 Dec 19	3600, 3600	2
19767........	f	2000 Dec 29	3000, 3000	2
20938........	e	1999 Dec 19	3600, 3600, 2400, 2400	4
23333........	e	1999 Dec 22	3600, 3600	2
23598........	b	1999 Jan 22	3600, 3600	2
23913........	b	1999 Jan 22	3600, 3600	2
24788........	f	2000 Dec 30	2400, 2400	2
26140........	b	1999 Jan 21	3600	1
26140........	f	2000 Dec 29	2400, 2400	2
26517........	f	2000 Dec 30	3000, 3000	2
27792........	e	1999 Dec 21	3600, 3600	2
28310........	b	1999 Jan 22	3600, 3600	2
28401........	e	1999 Dec 19	2400, 1800	2
31159........	c	1999 Mar 28	3600	1
31159........	f	2000 Dec 29	3000, 2400	2
32091........	e	1999 Dec 21	3600, 3600	2
32638........	f	2000 Dec 30	2400, 2400	2
33465........	e	1999 Dec 22	2400, 2400	2
36925........	c	1999 Mar 28	3600	1
38268........	e	1999 Dec 21	3600, 3600	2
38908........	b	1999 Jan 22	3600	1
38908........	f	2000 Dec 30	3000, 3000	2
39728........	e	1999 Dec 22	2400	1
46767........	b	1999 Jan 22	3600, 3600	2
46767........	b	1999 Jan 23	3600	1
49906........	c	1999 Mar 28	3600	1
49906........	f	2000 Dec 29	3000, 3000	2
55750........	c	1999 Mar 28	3600, 3000	2
56010........	c	1999 Mar 28	3600, 1200	2
56010........	c	1999 Mar 29	2400	1
57931........	d	1999 Sep 3	3600, 3600	2
58410........	a	1998 May 22	3600, 3600	2
70962........	e	1999 Dec 22	2400	1
71106........	e	1999 Dec 20	2400, 2400	2
72144........	e	1999 Dec 19	3600, 3600	2
72453........	e	1999 Dec 21	3600, 3600	2

[a] The run identification identifies the principal investigator (PI) and observers for each run: (a) PI: M. A. Bershady (UW allocation), Observers: M. A. Bershady & D. R. Andersen; (b) PI: M A. Bershady, J. S. Gallagher, L. S. Sparke, & E. M. Wilcots (UW allocation), Observer: D. R. Andersen; (c) PI: M. A. Bershady, J. S. Gallagher, L. S. Sparke, & E. M. Wilcots (UW allocation), Observers: D. R. Andersen & G. Madsen; (d) PI: M. A. Bershady (UW allocation), Observer: D. R. Andersen; (e) PI: D. R. Andersen (NOAO allocation), Observer: D. R. Andersen; (f) PI: M. A. Bershady & D. R. Andersen (UW allocation), Observer: D. R. Andersen.

(fibers) be used to sample 1 disk scale length. For galaxies with scale lengths less than $6''$, two overlapping DensePak positions offset by a half-fiber diameter were used. For scale lengths between $6''$ and $9''$, we used two DensePak positions offset to cover a $45'' \times 45''$ area, and for scale lengths between $9''$ and $12''$, we used three DensePak positions. The first two positions were offset $27''$ from each other. For the third position, DensePak was rotated, centered, and offset south of the first two positions. These three DensePak positions covered almost 1 arcmin^2. In order to observe the Hα line emission at 3 scale lengths and improve cosmic-ray rejection, we typically took two ~30 minute exposures at each position.

To center DensePak on our target we used a slit-viewing camera built into the fiber-mounting module known as WIFOE. Use of this camera involves inserting a pellicle for simultaneous viewing of the source and the rear-illuminated IFU. In this way, we aligned fiber 45 on a nearby guide star and then zeroed the telescope offsets. After moving to our target, we could see the target galaxy in the slit-viewing camera only if the galaxy had a high central surface brightness and the sky was dark and clear. If we saw the galaxy, we confirmed it was centered on fiber 45 and performed the first offset. If the galaxy was not visible, we performed a blind

offset. After guiding was established, we began observations. Typically, after two 30 minute exposures, guiding was turned off and the second set of telescope offsets was applied. After guiding was reestablished, we took our next two exposures. If a third position was required, we reacquired the nearby guide star and rotated DensePak. Since DensePak was not on the rotator axis, the star shifted a few arcsec as DensePak was rotated $90°$. After recentering the guide star on fiber 45, we moved DensePak back
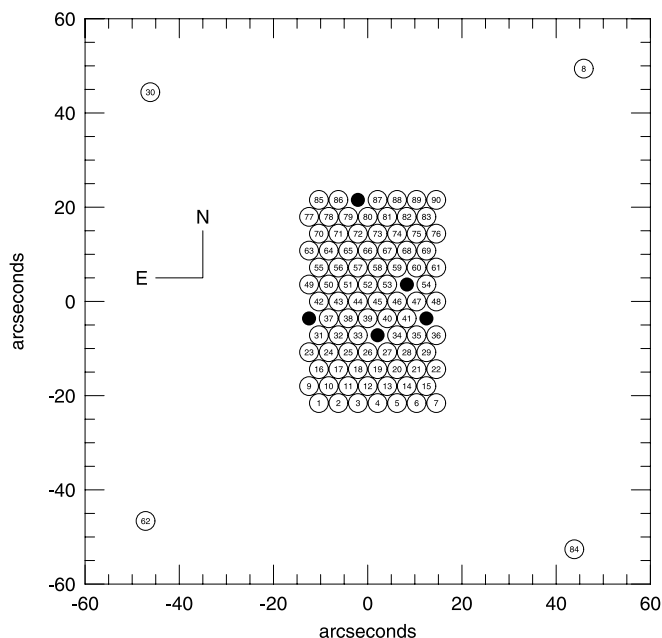
Fig. 4.—Schematic of DensePak in the telescope focal plane. Fibers are identified according to their position in the output slit. There are empty spaces in the slit between fibers 22–23, 26–27, 33–34, 36–37, 41–42, 53–54, and 86–87. Solid black disks mark broken fibers in the fiber bundle. Spatial orientation is for a zero rotation offset. Fibers are numbered in order of live fibers along the reconfigured output slit. This numbering scheme differs slightly from the DensePak manual.

to the source, applied the final telescope offset and took our final two exposures after reestablishing guiding. We found that rotating DensePak added up to 10 minutes of overhead to our observations; we therefore preferentially chose galaxies that required only two DensePak footprints to sample the disk out to 2.5 scale lengths.

We encountered problems with accurately positioning DensePak on-sky due to problems with the pellicle and nonguided offsets. For some of our observations, the pellicle did not properly align images in the slit-viewing camera, so our spectra were not centered as expected. However, when fitting velocity field models to multiple pointings, model centers were easily determined from the data. Hence, the unaligned pellicle did not diminish the quality of the data. However, inaccurate telescope offsets did complicate data handling. We performed tests at the telescope on the accuracy of our offsets by removing each offset in turn and recentering on the guide star. We discovered that the guide star moved as much as a fiber diameter (3″) after removing the telescope offsets. Therefore, we are forced to let telescope offsets be a free parameter in our model fits, thereby introducing extra fit parameters that could have been avoided if reliable offsets were possible. More tests are needed to determine an accurate method for applying telescope offsets using DensePak on WIYN.

At the beginning and end of each night, dome flats and bias frames were taken. We also observed thorium argon (ThAr) line lamps at the beginning of the night, before and after the dewar was filled, and again at the end of the night. The BSC dewar has a short hold time of only 12 hr and typically was refilled during the course of the night. We observed subpixel shifts of ~0.1 pixels in the centroids of the ThAr emission lines taken at different times. The largest shifts are seen between frames taken before and after dewar fills. When reducing spectra, we calibrated wavelengths using the ThAr frame taken closest to a given observation, within a period between filling of the dewar.

The quality of data from DensePak varied across the slit formed by the 90 fibers. In particular, comparisons of dome flat fluxes

showed the first eight fibers in the top of the slit had less than half the flux of most fibers (see Fig. 3 of Bershady et al. 2005). After field flattening, this low throughput was translated into greater values for the continuum noise in these fibers. We believe this poor performance may be due to the following: (1) fibers 1–8 undergo the tightest bend near the slit end of DensePak of all the fibers. Bershady et al. (2004) present evidence that this tight bend radius increases the focal ratio degradation of fibers for a similar integral field unit, SparsePak, thereby leading to greater losses in the spectrograph; (2) fibers 1–8 are at the top end of the DensePak slit. If the slit is not centered within the baffles at the spectrograph entrance, these fibers could suffer from further vignetting; (3) alternatively, these fibers may be otherwise over-stressed, e.g., because these fibers are on an outer face of the array (see Bershady et al. 2004). Data from fiber 1 were so poor that we did not include them when, for example, we stacked spectra to make synthetic line profiles (§ 5.2).

3.2. Nançay H i Observations

The Nançay telescope is a meridian transit-type instrument of the Kraus/Ohio State design, consisting of a fixed spherical mirror, 300 m long and 35 m high, a tiltable flat mirror (200 × 40 m), and a focal carriage moving along a 90 m long curved rail track, which allows the tracking of a source on the celestial equator for about 1 hr. Located in the center of France, it can reach declinations as low as $-39°$. It has an effective collecting area of roughly 7000 m^2 (equivalent to a 94 m diameter parabolic dish). Due to the elongated geometry of the mirrors, at 21 cm wavelength it has a half-power beam width (HPBW) of 3′.6 E–W × 22′ N–S for declinations below 30°; at higher declinations the N–S HPBW increases (see plot in Matthews et al. 2001). Typical system temperatures were ~40 K for our project. For a technical description of the Nançay decimetric radio telescope and the general methods for data handling and reduction see Theureau et al. (1998) and references therein.

Observations at Nançay of 23 sample galaxies were made in the periods 1999 March to August and 2001 January to June using a total of about 110 hr of telescope time. We obtained our observations in total power (position-switching) mode using consecutive pairs of 2 minute on-source and two-minute off-source integrations. Off-source integrations were taken at approximately 20′ east of the target position. The autocorrelator was divided into two pairs of cross-polarized receiver banks, each with 512 channels and a 6.4 MHz bandpass. This yielded a channel spacing of 2.64 km s^{-1}, for an effective velocity resolution of ~3.3 km s^{-1} at 21 cm, which was smoothed to a channel separation of 7.91 and a velocity resolution of 9.50 km s^{-1} during the data reduction, in order to search for faint features. The center frequencies of the two banks were tuned to the known redshifted H i frequency of the target.

4. BASIC PROCESSING

4.1. DensePak Reductions

Data were overscan and bias-corrected and trimmed using the NOAO IRAF package ccdproc. Since two or more frames were taken at each position, we calculated pairwise differences and statistical thresholds, pixel-by-pixel, of the expected variance (σ^2) due to read noise and shot noise. Pixels that were more than 5 σ brighter than the corresponding pixels on the other frames were flagged as cosmic rays and masked from the final, mean-combined, two-dimensional spectral image. This is preferable to removing cosmic rays after spectral extraction, which averages cosmic rays falling in pixels that are part of extracted apertures with good
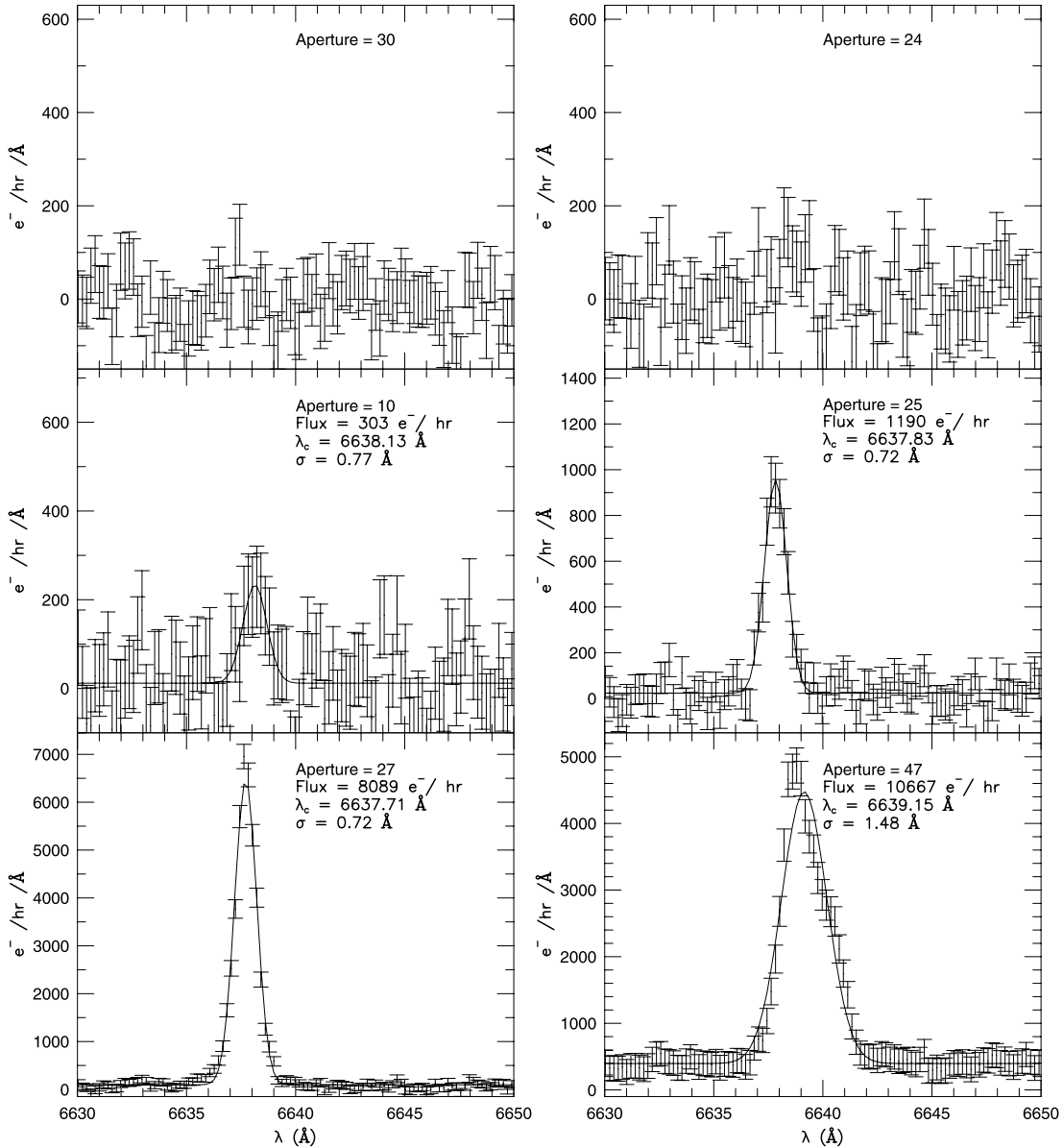
FIG. 5.—Hα emission-line profiles for 6 fibers selected from the first pointing of PGC 14564. Fiber 30 was a sky fiber and illustrates the typical background fluctuations. The solution for a Gaussian Hα emission-line in Fiber 24 (*upper right panel*) did not meet the S/N criterion: $\zeta \equiv f_G/\sigma_{cont.}/(2\sigma_G)^{1/2} > 5$. For the emission-line in aperture 10 (*left, middle panel*), $\zeta = 8$. The Hα emission-line for aperture 25 (*middle right panel*) was typical for most observed galaxies. Aperture 27 (*bottom left*) shows very strong Hα emission for our survey. The Hα profile in aperture 47 (*lower right panel*) was highly skewed, showing signs of bimodality.

data from other pixels in same spectral channel. Following cosmic-ray cleaning, basic spectral extraction, flattening, wavelength calibration, and sky subtraction were done using IRAF dohydra. Extracted one-dimensional spectra were field-flattened with dome flats and wavelength-calibrated using ThAr emission spectra. Finally, the four sky spectra were averaged and the mean sky spectrum was subtracted from the other 86 spectra.

Once spectra were processed with IRAF dohydra, we identified extracted Hα emission-line characteristics. Our algorithm measured Gaussian fluxes, widths, centers, and centroid errors for lines in a given spectral interval. Most emission-lines in our data were symmetric and were well fitted by a single Gaussian. Some Hα profiles sampled by fibers within a fiber radius of the galaxy center were skewed or even bimodal as would be expected when the fiber diameter is larger than the local dynamical scale. Since the fraction of such lines was small, we flagged these lines during visual inspection after running our automated line fitting

algorithm and do not cite the fit results later. While Beauvais & Bothun (1999) found the best fits to a variety of different simulated line profiles were obtained with Vogt profiles (a combination of Gaussian and Lorentzian profiles), they noted that Gaussian fits yielded comparable results for signal-to-noise (S/N) ratios greater than 20. A similar conclusion was reached by Courteau (1997), who measured intensity-weighted centroids. Our typical Hα lines had high S/N, and a visual inspection of the fits made it clear that Gaussian profiles were sufficient to describe most emission lines.

Since the S/N of each channel in the spectra is important for accurate profile fitting, we iteratively established measurement errors for each channel. We begin by calculating an iterative clipped mean and standard deviation within a 30 Å window containing the emission line. We used a very tight clipping criterion: All channels with counts greater than the standard deviation were rejected, repeating until the number of channels did not decrease

TABLE 3
GAUSSIAN FITS TO Hα EMISSION LINES: FIRST POINTING OF PGC 2162

Name	Fiber	Pointing (arcsec)	Offset West (arcsec)	Offset North (Å)	λ_C (Å)	$\Delta\lambda_C$ (e^{-1} hr^{-1})	f_G (Å)	σ_G (e^{-1} hr^{-1} res^{-1})	$\sigma_{cont.}$
PGC 2162	1	1	−21.9	−21.5	...	...	...	...	97
	2	1	−17.7	−21.5	...	...	...	...	21
	3	1	−13.6	−21.5	...	...	...	...	13
	4	1	−9.4	−21.5	...	...	...	...	10
	5	1	−5.29	−21.52	6682.08	0.07	520	0.33	10
	6	1	−1.14	−21.52	6682.23	0.05	933	0.43	10
	7	1	3.01	−21.52	6682.33	0.03	1627	0.38	12
	8	1	34.3	49.5	...	...	...	...	7
	9	1	−24.0	−17.9	...	...	...	...	11
	10	1	−19.82	−17.92	6681.83	0.06	745	0.46	7
	11	1	−15.67	−17.92	6681.68	0.03	1434	0.46	7
	12	1	−11.52	−17.92	6681.86	0.07	584	0.46	7
	13	1	−7.37	−17.92	6681.96	0.10	272	0.39	7
	14	1	−3.22	−17.92	6682.19	0.05	745	0.40	7
	15	1	0.93	−17.92	6682.37	0.02	1719	0.44	7
	16	1	−21.89	−14.33	6681.83	0.11	590	0.63	7
	17	1	−17.74	−14.33	6681.62	0.04	917	0.43	7
	18	1	−13.59	−14.33	6681.79	0.05	774	0.48	7
	19	1	−9.44	−14.33	6681.94	0.04	847	0.37	7
	20	1	−5.29	−14.33	6681.98	0.05	585	0.33	8
	21	1	−1.14	−14.33	6682.20	0.01	4074	0.50	8
	22	1	3.01	−14.33	6682.41	0.01	4215	0.44	6
	23	1	−23.97	−10.74	6680.97	0.24	825	1.31	7
	24	1	−19.82	−10.74	6681.55	0.03	1288	0.44	6
	25	1	−15.67	−10.74	6681.49	0.15	595	0.83	6
	26	1	−11.52	−10.74	6681.78	0.03	1151	0.41	6
	27	1	−7.37	−10.74	6681.99	0.05	982	0.53	8
	28	1	−3.22	−10.74	6682.19	0.02	1880	0.46	7
	29	1	0.93	−10.74	6682.27	0.01	3638	0.41	7
	30	1	−57.7	44.5	...	...	...	...	5
	31	1	−21.89	−7.14	6681.51	0.03	1092	0.40	6
	32	1	−17.74	−7.14	6681.64	0.05	860	0.48	6
	33	1	−13.59	−7.14	6681.70	0.04	1028	0.47	6
	34	1	−5.29	−7.14	6681.93	0.01	3037	0.42	6
	35	1	−1.14	−7.14	6682.09	0.01	3886	0.42	7
	36	1	3.01	−7.14	6682.57	0.01	2754	0.44	8
	37	1	−19.82	−3.55	6681.30	0.10	477	0.62	6
	38	1	−15.67	−3.55	6681.62	0.03	1212	0.48	6
	39	1	−11.52	−3.55	6681.72	0.01	2244	0.40	6
	40	1	−7.37	−3.55	6681.80	0.01	4608	0.41	7
	41	1	−3.22	−3.55	6681.88	0.01	5839	0.42	11
	42	1	−21.89	0.05	6681.74	0.07	533	0.48	6
	43	1	−17.74	0.05	6681.79	0.04	645	0.35	6
	44	1	−13.59	0.05	6681.70	0.01	1809	0.41	6
	45	1	−9.44	0.05	6681.76	0.01	3752	0.41	7
	46	1	−5.29	0.05	6681.79	0.01	4946	0.40	9
	47	1	−1.14	0.05	6681.98	0.02	1934	0.43	21
	48	1	3.01	0.05	6683.06	0.01	3267	0.41	14
	49	1	−23.97	3.64	6681.73	0.06	474	0.42	6
	50	1	−19.82	3.64	6681.70	0.05	738	0.48	6
	51	1	−15.67	3.64	6681.91	0.07	698	0.65	6
	52	1	−11.52	3.64	6681.79	0.01	2941	0.40	5
	53	1	−7.37	3.64	6681.90	0.01	5264	0.42	7
	54	1	0.93	3.64	6682.74	0.01	3594	0.50	13
	55	1	−21.89	7.23	6681.83	0.04	471	0.32	6
	56	1	−17.74	7.23	6681.87	0.06	303	0.34	6
	57	1	−13.59	7.23	6681.90	0.03	918	0.36	6
	58	1	−9.44	7.23	6681.98	0.01	2744	0.43	7
	59	1	−5.29	7.23	6682.20	0.01	5919	0.40	8
	60	1	−1.14	7.23	6682.40	0.01	4598	0.44	8
	61	1	3.01	7.23	6682.92	0.01	3820	0.43	7
	62	1	−58.7	−46.5	...	...	...	...	5
	63	1	−24.0	10.8	...	...	...	...	7
	64	1	−19.82	10.83	6681.87	0.04	480	0.32	6

TABLE 3—*Continued*

Name	Fiber	Pointing (arcsec)	Offset West (arcsec)	Offset North (Å)	λ_C (Å)	$\Delta\lambda_C$ (e^{-1} hr^{-1})	f_G (Å)	σ_G (e^{-1} hr^{-1} res^{-1})	$\sigma_{cont.}$
PGC 2162	65	1	−15.67	10.83	6681.93	0.03	496	0.28	7
	66	1	−11.52	10.83	6681.99	0.04	829	0.43	6
	67	1	−7.37	10.83	6682.20	0.03	1330	0.49	6
	68	1	−3.22	10.83	6682.37	0.02	2225	0.44	8
	69	1	0.93	10.83	6682.69	0.02	1763	0.38	7
	70	1	−21.89	14.42	6681.68	0.13	842	1.04	7
	71	1	−17.7	14.4	...	...	...	...	6
	72	1	−13.59	14.42	6682.05	0.06	383	0.31	6
	73	1	−9.44	14.42	6682.21	0.04	633	0.31	7
	74	1	−5.29	14.42	6682.27	0.06	734	0.45	7
	75	1	−1.14	14.42	6682.63	0.02	2145	0.46	8
	76	1	3.01	14.42	6682.79	0.02	2223	0.39	7
	77	1	−23.97	18.02	6682.22	0.18	352	0.69	6
	78	1	−19.82	18.02	6682.08	0.13	671	0.78	8
	79	1	−15.7	18.0	...	...	...	...	7
	80	1	−11.5	18.0	...	...	...	...	7
	81	1	−7.37	18.02	6682.26	0.05	628	0.36	7
	82	1	−3.22	18.02	6682.48	0.04	1160	0.47	8
	83	1	0.93	18.02	6682.69	0.03	1513	0.44	7
	84	1	32.3	−52.5	...	...	...	...	6
	85	1	−21.9	21.6	...	...	...	...	9
	86	1	−17.7	21.6	...	...	...	...	7
	87	1	−9.4	21.6	...	...	...	...	8
	88	1	−5.3	21.6	...	...	...	...	8
	89	1	−1.14	21.61	6682.53	0.06	778	0.44	8
	90	1	3.01	21.61	6682.73	0.04	681	0.30	8

Note.—Table 3 is available in its entirety in the electronic edition of the *Astrophysical Journal Supplement*. A portion is shown here for guidance regarding its form and content.

further. This procedure removed almost all effects of emission lines, imperfectly subtracted sky lines, and residual cosmic rays from the continuum mean and standard deviation. We normalized the standard deviation of the iteratively clipped data by the standard deviation of a Gaussian distribution, which also had been truncated at 1 σ. With the continuum standard deviation, $\sigma_{cont.}$, established, we assumed remaining errors on channel counts were based on Poisson counting errors. Therefore, the error on each channel, σ_i, was calculated as follows:

$$\sigma_i = \left[\sigma_{cont.}^2 + (\text{Counts}_i - \text{Counts}_{cont.})\right]^{1/2}, \qquad (1)$$

where all counts were calculated in e^- pixel^{-1}, Counts$_i$ represented the counts for channel i, and Counts$_{cont.}$ represented the iterative mean calculated in the 200 Å window.

Once electron counts and the initial estimates of the standard deviations had been calculated for every channel, we used the Marquardt-Levinson algorithm to fit a Gaussian profile plus a linearly varying background to the line within the selected region. We then subtracted this best-fit spectrum within the window and recalculated the standard deviation following the same procedure described above. Then we refit the data and extract the Gaussian amplitude, center (λ_C) and width (σ_G) from the fit. The area beneath the curve yields the flux (f_G). The error on the centroid (σ_{λ_C}) was obtained from the covariance matrix.

We found that features that had Gaussian fits that did not reach the S/N threshold $f_G/\sigma_{cont.}/(2\sigma_G)^{1/2} > 5$ were also not identified as emission lines by visual inspection. We also required the width of the line must be equal to or greater than the resolution element. Finally, as already noted, we discarded lines that, based on visual inspection, were skewed, required multiple Gaussian profiles, or formally met the S/N and width requirements but nonetheless did

not look plausible. Figure 5 shows a sample of the output with Gaussian fits chosen for their range of properties: an example of sky continuum, a line that did not meet the S/N threshold, a weak line that did have sufficient S/N, typical, strong, and skewed lines.

Table 3 contains a sample of the DensePak line fits for the first pointing of PGC 2162. The line fits tables for all 39 galaxies are available in electronic form. Tabulated offsets refer to the fiber positions west and north of the kinematic center based on our model fits to the velocity fields described in the relevant forthcoming paper in this series, and the astrometric information regarding relative fiber positions described in § 3.1.

We followed this procedure for the sample of 39 galaxies, or 8280 individual spectra. 6000 (72.5%) of the spectra showed clear emission lines that were detected and well fitted by the algorithm based on visual inspection. 1875 (22.6%) of the spectra had no detectable emission lines. 368 of these were sky spectra. Visual inspection flagged 46 (0.6%) spectra with potential emission lines that were undetected by the algorithm. All of these had low S/N and indeed simply may not have met the S/N criteria. 98 (1.2%) of the spectra were asymmetric, showing either a high degree of skew or requiring multiple components. A single Gaussian profile is not a good fit to these profiles; widths and centroids are quite possibly in error. They were excluded from Table 3. As stated above, these fibers are located very close to the center. In most cases, they are within a fiber radius of the center. 48 (0.6%) of the spectra had fits but were ruled out by visual inspection. Most of these false positives are weak cosmic rays or a result of some residual curvature in the spectra that was not removed through flat-fielding. These are not included in Table 3. The remaining 213 (2.6%) of spectra had questionable fits. These algorithm detections are at a low S/N, and may not have been detected as lines by visual inspection. Some of these questionable fits may be

TABLE 4

H I Parameters from Nançay Observations

PGC	rms[a] (mJy)	S/N[b]	$I_{\rm H\,I}$[c] (Jy km s^{-1})	W_{50}[d] (km s^{-1})	W_{20}[e] (km s^{-1})	$V_{\rm H\,I}$[f] (km s^{-1})	$\sigma_{V_{\rm H\,I}}$[g] (km s^{-1})	log $M_{\rm H\,I}$[h] (log $M_\odot$)
03512	5.82	...	...	...	...	5436	...	...
08941	5.31	6.69	4.72	162	...	9447	5.6	10.16
14564	2.96	26.33	10.06	176	202	3483	2.2	9.71
15531	5.60	5.63	4.23	157	197	5552	12.9	9.74
16274	3.74	...	...	...	...	8883	...	...
19767	4.21	10.34	5.35	141	164	5136	5.4	9.77
23598	2.80	10.41	2.57	119	139	7478	4.9	9.78
23913	3.52	34.82	4.39	33	57	6330	1.6	9.87
24788	2.86	11.56	4.63	161	194	7545	5.8	10.04
26140	1.79	...	...	...	...	8760	...	...
28310	2.7	7.55	2.65	141	153	5905	5.1	9.59
31159	4.9	3.26	2.32	190	199	5781	10.7	9.51
32091	3.03	...	...	...	...	2511	...	...
32638	2.80	5.45	1.83	172	229	6527	15.8	9.51
33465	4.41	...	...	...	...	5935	...	...
36925	7.67	...	...	...	...	6826	...	...
38908	3.87	13.84	7.61	195	221	7084	4.2	10.20
39728	1.97	8.81	2.08	145	196	2316	9.1	8.67
46767	2.89	8.47	4.06	276	335	8065	10.4	10.07
56010	4.80	4.78	4.80	63	160	4469	23.2	9.60
57931	6.09	...	...	...	...	9280	...	...
58410	5.21	5.09	4.44	256	326	9055	18.9	10.18
72453	3.24	11.26	4.38	160	194	9932	6.0	10.26

[a] Root mean squared noise level of the spectrum.
[b] Ratio of peak line flux to the rms noise level. During reduction, data were smoothed to an effective velocity resolution of 9.5 km s^{-1}.
[c] Integrated line flux.
[d] Velocity width at 50% the peak line flux. According to Fouqué et al. (1990), the uncertainty in W_{50} is $2\sigma_{V_{\rm H\,I}}$.
[e] Velocity width at 20% the peak line flux. According to Fouqué et al. (1990), the uncertainty in W_{20} is $3\sigma_{V_{\rm H\,I}}$.
[f] Heliocentric central radial velocity of a line profile in the optical convention.
[g] Uncertainty in $V_{\rm H\,I}$, is $\sigma_{V_{\rm H\,I}} = 4R^{1/2}P_W^{1/2}(S/N)^{-1}$, where R is the instrumental resolution (15.6 km s^{-1}), $P_W = (W_{20} - W50)/2$ (Fouqué et al. 1990).
[h] Total H I mass, $M_{\rm H\,I} = 2.356 \times 10^4 D^2 I_{\rm H\,I}$, where D is the distance calculated assuming $H_0 = 75$ km s^{-1} Mpc^{-1}.

cosmic rays. Most are just emission lines that just barely meet the detection threshold.

4.2. H I Reductions

We reduced our H I spectra using the standard Nançay spectral line reduction packages available at the Nançay site. With this software we subtracted baselines (generally third order polynomials), averaged the two receiver polarizations, and applied a declination-dependent conversion factor to convert from units of $T_{\rm sys}$ to flux density in mJy. The $T_{\rm sys}$-to-mJy conversion factor is determined via a standard calibration relation established by the Nançay staff through regular monitoring of strong continuum sources. This procedure yields a calibration accuracy of ~15%. In addition, we applied a flux scaling factor of 1.26 to our spectra based on statistical comparisons (see Matthews et al. 1998, 2001) of Nançay survey data of samples of late-type spirals with past observations of these galaxies made at Nançay and elsewhere.

From the 23 galaxies observed with Nançay from the two campaigns (1999 March–August and 2001 January–June), 18 had sufficient signal to measure line widths and integrated H I fluxes (Table 4). The line widths listed in Table 4 have not been corrected for redshift stretch. Rest-frame line widths should be reduced by a factor $(1 + z)^{-1}$.

4.3. H I Values from the Literature

H I observations from the literature were drawn from the LEDA extragalactic database (Paturel et al. 2003) to complement Nançay observations. Corrections were made to the raw H I data to account for velocity resolution and inhomogeneity of the various original references to produce velocity widths measured on a common system using the optical convention ($v = c\Delta\lambda/\lambda$) at 20% and 50% of the peak flux. These corrected W_{20} and W_{50} line widths are tabulated for 28 sample galaxies in Table 5. H I observations either from the Nançay observations described above or from the LEDA database exists for 38 of the 39 sample galaxies. There are 10 galaxies with W_{50} line widths from both Nançay observations and the literature, and the measurements are in good agreement. The mean difference in Nançay versus LEDA W_{50} line widths is 1.7 km s^{-1}; the greatest difference in these W_{50} values (15.3 ± 12.6 km s^{-1}) is consistent with the errors. Three of the six galaxies with both Nançay and literature W_{20} line widths show discrepancies greater than 20 km s^{-1}. In these cases, the relatively low S/N of the Nançay observations for PGC 39728, PGC 46767, and PGC 58410 have led to an overestimate of W_{20} (see § 5.4.1).

5. Hα LINE WIDTHS

Creating Hα line width profiles from DensePak observations is a computationally straightforward process, as described below, but it is necessary to ensure these line widths are physically meaningful. The filling factor of DensePak is only 45% (factoring in the 4 dead fibers plus the highly vignetted fiber 1). In addition to the low filling factor, Hα may exist at radii beyond the 3 scale lengths typically covered by the DensePak observations. Further, since the sample is nearly face-on, the "turbulent" component of the spatially integrated line width is critical to understand. Therefore, we first characterize the spatially resolved Hα line widths, as observed with DensePak. After describing the construction of the

TABLE 5
H i Line Widths from Paturel et al. (2003)

PGC	W_{20} (km s^{-1})	$\sigma_{W_{20}}$ (km s^{-1})	W_{50} (km s^{-1})	$\sigma_{W_{50}}$ (km s^{-1})
03512...............	204.9	10.7	182	8.1
05345...............	52.49	13.32	27.05	9.7
05673...............	147.75	12.85	134.05	9.7
06855...............	136.5	10.7	115.7	8.1
07826...............	96.08	8.32	85.4	8.24
08941...............	157.22	12.85	147.32	6.86
14564...............	198.93	7.39	179.64	4.62
19767...............	147.9	15.86	137.14	11.94
20938...............	...	...	169.61	8.5
23333...............	139.12	13.28	134.42	7.1
23598...............	...	...	121.37	10.49
23913...............	...	...	47.37	12.51
24788...............	...	...	147.76	17.61
26517...............	126.5	10.7	125.7	8.1
27792...............	...	...	129.87	8.47
28401...............	59.5	10.7	37.7	8.1
33465...............	285.9	15.86	239.14	11.94
36925...............	149.9	15.86	138.14	11.94
38268...............	183.33	11.97	162.92	10.02
39728...............	163.28	7.08	148.96	7.46
46767...............	292.9	15.86	253.14	11.94
55750...............	108.05	6.41	92.61	16.26
57931...............	176.41	12.54	170.19	11.78
58410...............	248.9	15.86	231.32	8.68
70962...............	242.35	6.03	209.09	9.73
71106...............	266.78	8.46	236.86	7.34
72144...............	...	...	125.31	6.97
72453...............	179.2	13.28	157.3	10.02

DensePak Hα line width profiles, we compare the DensePak Hα line width profile to one generated from narrowband Hα imaging. We also comment briefly on the shape and width of the H i and Hα profiles, with a more detailed analysis presented in the relevant forthcoming paper in this series.

5.1. Spatially Resolved DensePak Line Widths

The projected Hα velocity widths from individual fibers vary little with radius, when considering the sample taken as a whole. Variations do exist, however, between and within galaxies; these variations are explored in a future paper. The sample-mean near-constancy with galactic radius is similar to what has been found for individual, nearly face-on disk galaxies in neutral gas (NGC 628, NGC 1058, and NGC 3938; van der Kruit & Shostak 1982, 1984; Dickey et al. 1990), molecular gas (NGC 628 and NGC 3938; Combes & Becquaert 1997), and ionized gas (NGC 3938 and NGC 5668; Jiménez-Vicente et al. 1999; Jiménez-Vicente & Battaner 2000; NGC 3359, Rozas et al. 2000; NGC 6951, Rozas et al. 2002). The reasons for this gross similarity of the near-constancy with radius of different phases of the ISM is outside the scope of this paper, but we do note that some radial dependence in the neutral gas is observed in some galaxies (Shostak & van der Kruit 1984; Kamphuis & Sancisi 1993), and variations are also seen in the ionized gas in some cases in our sample, albeit over different radial ranges. Our distribution median, out of 6000 fiber samples with emission lines well characterized by a single Gaussian across 39 galaxies in our sample is $17.9^{+3.5+8.1}_{-2.9-5.7}$ km s^{-1}, where the two sets of "errors" include 50% and 80% of the distribution. These values are corrected for instrumental broadening only. They are consistent in value and distribution for what has been observed in two other, nearby spirals NGC 3938 and NGC 5668
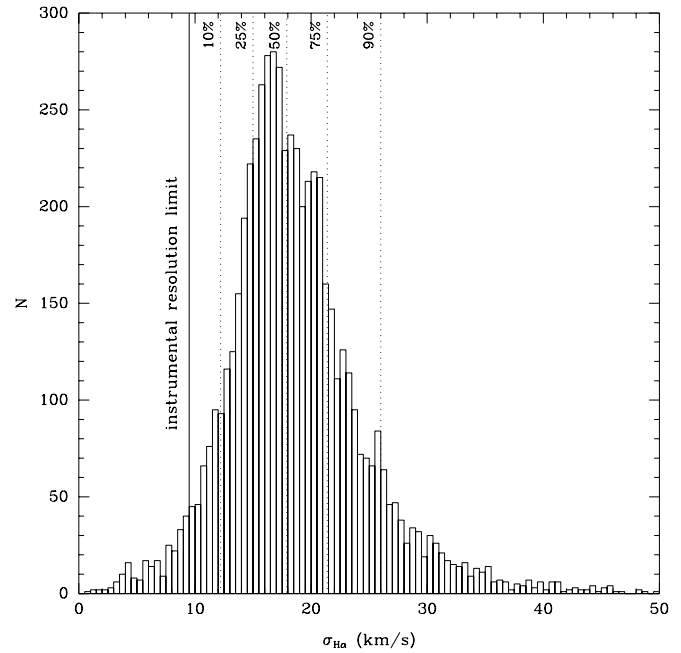
Fig. 6.—Distribution of Hα emission-line velocity widths (σ), as observed for the entire sample of 39 galaxies, corrected for instrumental broadening. The instrumental resolution limit and integral distribution percentiles are indicated. The instrumental resolution is well below the peak of the observed distribution.

(Jiménez-Vicente et al. 1999; Jiménez-Vicente & Battaner 2000; Rozas et al. 2000, 2002) and are roughly 2–3 times the dispersion measured in either neutral (van der Kruit & Shostak 1982, 1984) or molecular gas (Combes & Becquaert 1997) for relatively small samples of galaxies. The tightness of our sample distribution is shown in Figure 6. The largest values that skew the distribution slightly are seen primarily at the center of galaxies with steep inner rotation curves. While beam smearing appears to affect these values, the effect is small and correctable, and it does not adversely influence our results here.

5.2. Spatially Integrated DensePak Line Widths

After taking the steps as described in § 4.1 of extracting the spectra and fitting Gaussian line profiles, we generated "spatially integrated" line widths—what we refer to here also as "synthetic line profiles." We co-added either the individual extracted spectra (channel by channel), or we co-added the individual fitted Gaussian line profiles for those spectra where fits were possible. When combining these data or fitted profiles, we maintained a count of the number of independent fiber positions. An on-sky location was assigned to each fiber based on the DensePak geometry and telescope offsets determined via velocity-field fitting (presented in a future paper). The location of fibers from different pointings were checked for overlap. If there was an overlap between fibers, the relevant fiber flux was scaled such that the combined spectra gave equivalent spatial sampling to nonoverlapping areas. Specifically, for each fiber we determined the number of fibers in a hexagonal area inscribed within a 6″.3 radius circle centered on the fiber and compared this to the expected number in nonoverlapping regions (e.g., 7 fibers for the middle of the array). We did not include spectra from fiber 1, as they suffered from extremely low S/N.

5.3. Spatially Integrated Line Widths from Narrowband Imaging

To test whether the Hα line width profiles derived from DensePak observations were valid representations of the matter
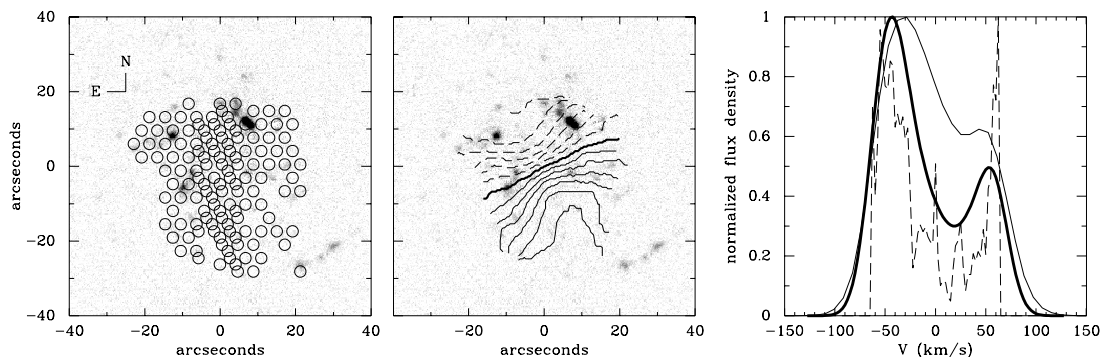
FIG. 7.—*Left*: Narrowband Hα image of PGC 38268 with overlay of the DensePak fiber locations in which Hα was detected. Aside from the Hα flux missed at large radii due to the limited field of view of Densepak, the IFU successfully detected Hα across the galaxy even at locations in which the imaging data do not yield discrete Hα detections. *Center*: The DensePak Hα velocity field overlaid on the narrowband Hα image of PGC 38268. *Right*: Normalized flux density of the PGC 38268 Hα line profile. Jagged dashed line is the raw line profile obtained by convolving the velocity field model and the Hα flux from the narrowband image. The heavy solid line is this same profile convolved with a Gaussian with 20 km s^{-1} width (which corresponds to the measured mean emission line width before instrumental correction was applied). The thin solid line is the DensePak line profile obtained by summing the individual Gaussian fits. The simulated profile has virtually the same width as the data and shows a qualitatively similar asymmetry profile.

and velocity distribution of the ionized gas, we constructed a line width profile from the narrowband Hα image of one galaxy in our sample, PGC 38268, for comparison.

5.3.1. *Observations*

PGC 38268 was observed in narrowband filters using the SPIcam camera at the Apache Point Observatory (APO) 3.5 m telescope on 2002 April 11. SPIcam is an imager equipped with a 2048 × 2048 pixel SITe back-illuminated CCD that has a 4′.8 field of view. In the standard mode of operation (2 × 2 binning) SPIcam has an effective plate scale of 0″.281/pixel. Rest-frame Hα and a 6629 Å off-band filter come from a set owned by P. Hodge. SPIcam is designed to accommodate 3 × 3 inch filters, so the 2 × 2 inch narrowband filters consequently reduce SPIcam's effective field of view (FOV).

The recession velocity of PGC 38268 shifted the Hα emission into the 6629 Å narrowband filter. The Hα and 6629 Å filters make an ideal pair of filters for narrowband imaging because the filters' transmission curves are virtually the same in width and shape. Since the night was not photometric, no attempt was made to collect flux standards. Exposures in each band totaled 10 minutes.

5.3.2. *Reductions*

We used standard IRAF tasks to process images (overscan correction, bias subtraction, and flat-fielding). Images were trimmed to include only the unvignetted FOV. The standard IRAF cosmic-ray cleaning task was augmented using information from neighboring pixels, thus enhancing the cleaning of extended cosmic-ray events and detector flaws.

Once individual data frames were fully processed, the sky background was calculated using an iteratively clipped mean and subtracted from all frames. On- and off-band images were registered using 5 field stars. Since the ratio of fluxes in on versus off-band for these stars were in agreement with the predicted ratio based on the filter transmission curves, we used the ratio expected from the transmission curves to scale the images and subtract frames. The Hα narrowband image of PGC 38268 with the overlay of DensePak fibers in which Hα was detected is shown in the first panel of Figure 7. While DensePak does not detect all the Hα flux because the two clumps of Hα to the SW and the faint clumps to the north were not covered by the DensePak array, DensePak is able to detect very faint levels of Hα emission that are not visible in the image.

5.3.3. *A Comparison of Line Profiles*

We use this Hα narrowband image of PGC 38268 to produce a line width profile. To do this, we assign a velocity to each position in the image. Following the fitting procedure outlined in Andersen et al. (2001), a best-fit velocity field was determined from the DensePak data. The second panel of Figure 7 shows the observed velocity field from the DensePak data overlaid on the narrowband image of PGC 38268. The best-fit analytic model to this observed velocity field was then used to assign a velocity to each pixel of the narrowband image. The resultant profile (Fig. 7, *dashed line*) was then smoothed by a 20 km s^{-1} width Gaussian profile (Fig. 7, *solid line*). This smoothing corresponds to the median measured Hα line width in spectra of individual DensePak fibers.

When the line width derived from the DensePak data if overlaid on this image (Fig. 7, *dotted line*), good agreement is observed between the smoothed profile and the DensePak profile. W_{20}, the velocity width measured at 20% of the peak velocity, when measured from the profile derived from the Hα image is 152 km s^{-1} and when measured from the profile created directly from the DensePak spectra is 162 km s^{-1}. A difference of 5 km s^{-1} in the width of the smoothing Gaussian used to smooth the line profile can account for this difference. The more striking discrepancy is between the peak flux levels in the two halves of the profile. The ratio of fluxes from the DensePak data is 0.6, while the ratio is 0.5 when measured from the Hα image. This agrees qualitatively with the relative positions of Hα emission and the DensePak footprint: More Hα flux falls between fibers in the receding (northern) half of the velocity field. Finally, the difference in velocity between the two peaks is slightly greater in the data from the Hα imaging. This is consistent with the nondetection of Hα at large radii and velocities in the DensePak data.

Overall, however, we conclude the DensePak-derived integrated line width is likely an excellent approximation.

5.4. *Synthetic* Hα *Line Profiles*

We present these synthetic line profiles for both the raw data and the summed, best-fit Gaussian profiles in Figure 8, along with an overlay of the DensePak observations on the *R*-band images. As can be seen by direct visual inspection, the line profile width and shape is very similar for the raw and Gaussian summations. The smoothing of the data with the Gaussian summation does not quantitatively alter low-order moments of the integrated line profiles. For example, we find the variation of the skew, or
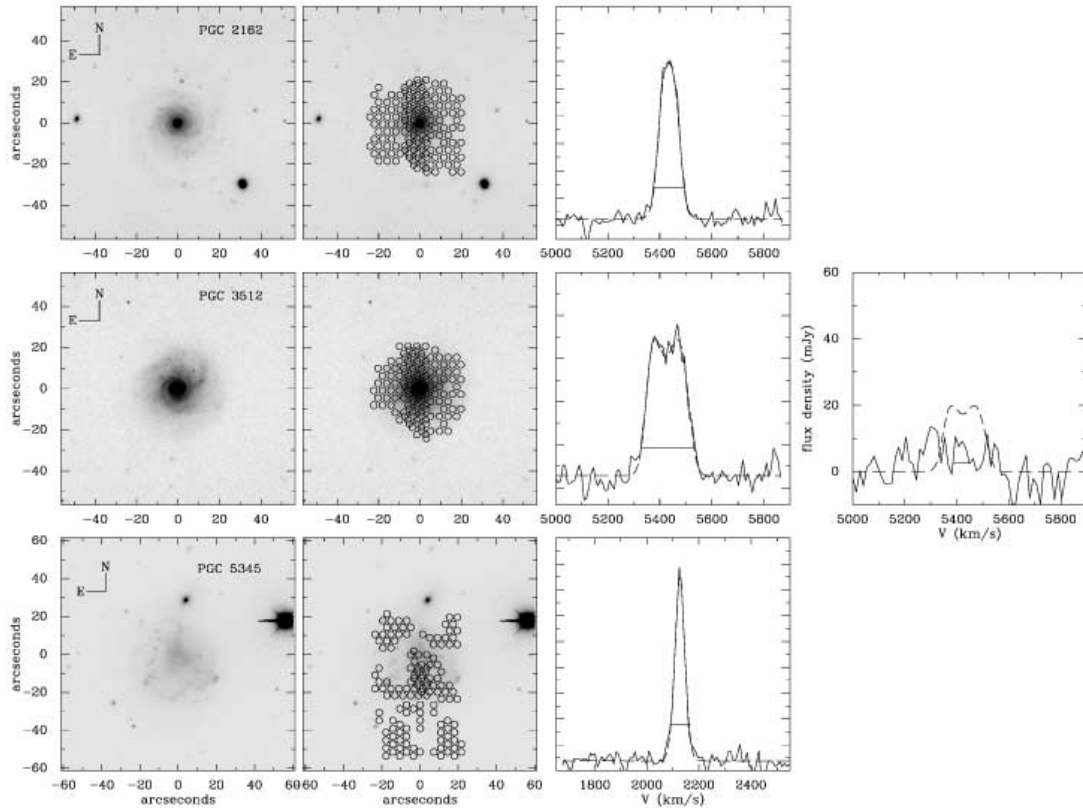
Fig. 8.—*Leftmost column*: Images of the 39 sample galaxies with overlays of the DensePak fibers in which Hα is detected. *Central column*: Hα velocity profiles from the DensePak observations. The Hα flux densities are plotted against heliocentric velocities. No units are given on the flux densities because nights were generally clear but not photometric, nor were flux-standards observed. The smoother profiles are sums of Gaussian fits to individual fiber Hα profiles. These "Sum of Gaussian" profiles agree well with the raw data. Flux from fibers with centers that fall within a fiber radii are averaged. W_{20}, the width of the Hα lines at 20% the peak flux is illustrated by a horizontal line in the plots. *Rightmost column*: The H I flux densities from Nançay 21 cm observations (where available) vs. heliocentric velocities. The smooth curve is again the Hα "Sum of Gaussian" profile scaled to the H I peak flux. W_{20}, the width of the H I lines at 20% the peak flux is illustrated by a horizontal line in the plots.

lopsidedness, of the line profile between raw and Gaussian summations is less than the observational error, and they are identical in the mean.

A comparison between the H I and Hα profiles are also presented in Figure 8, where the data are available. In general there is very good agreement between the widths of the H I and Hα profiles. Using the Gaussian fits to the individual Hα spectra, we constructed a width by finding the maximum difference in centroid velocities. We compared this width to the 31 H I W_{20} measures and found a constant offset between the relations. The H I line widths are 23 ± 20 km s^{-1} broader than the Hα velocity "widths" as defined above, roughly comparable to the ∼18 km s^{-1} spatially resolved line widths of the Hα emission lines. Only two of these galaxies, PGC 56010 and PGC 70962, showed significantly larger differences in velocity widths. As noted below, only half the disk of PGC 56010 is covered with DensePak pointings. Similarly, we only cover the inner starbursting region of PGC 70962, but we suspect the width of the H I profile may be dominated by the especially broad emission lines observed in the Hα spectra and may not reflect the kinematics of the galaxy. Further comparisons of H I and Hα line widths are in a forthcoming paper.

5.4.1. *Notes to Individual Galaxies*

For galaxies with both DensePak Hα and Nançay H I line profiles shown in Figure 8, we normalized the peak fluxes of the Hα line profiles generated from the sum of individual Gaussian

fits to the H I line profile peak flux for comparison. Here we take note of the features observed in the line widths for galaxies with both DensePak Hα and Nançay H I data.

PGC 3512.—No H I flux from the source was detected.

PGC 08941.—Nançay observations were severely affected by radio interference, but no H I flux was detected at the recession velocity of the source.

PGC 14564.—H I and Hα line profiles are very similar. The only notable difference is the slightly broader width of the Hα profile.

PGC 15531.—S/N of the H I line width is low, but the shape of the line profiles are very similar.

PGC 16274.—Nançay observations had a poor base-line, making a comparison between Hα and H I line widths difficult.

PGC 19767.—Hα data exhibit a strong asymmetry in the line profile that is not observed in the H I data.

PGC 23598.—Hα and H I line widths are equivalent, and both profiles are asymmetric. The detailed shapes of the profiles, however, are markedly different.

PGC 23913.—Neither line profile shows evidence of significant rotation.

PGC 24788.—H I data have a slightly broader line width and is double-peaked, while the Hα profile is not.

PGC 26140.—There is a strong mismatch between Hα and H I line profiles, with little H I signal at the source redshift, but a possible, narrow peak blueshifted by 300–350 km s^{-1}. Within the Nançay beam lies PGC 26140 (2″.4 separation), an elliptical
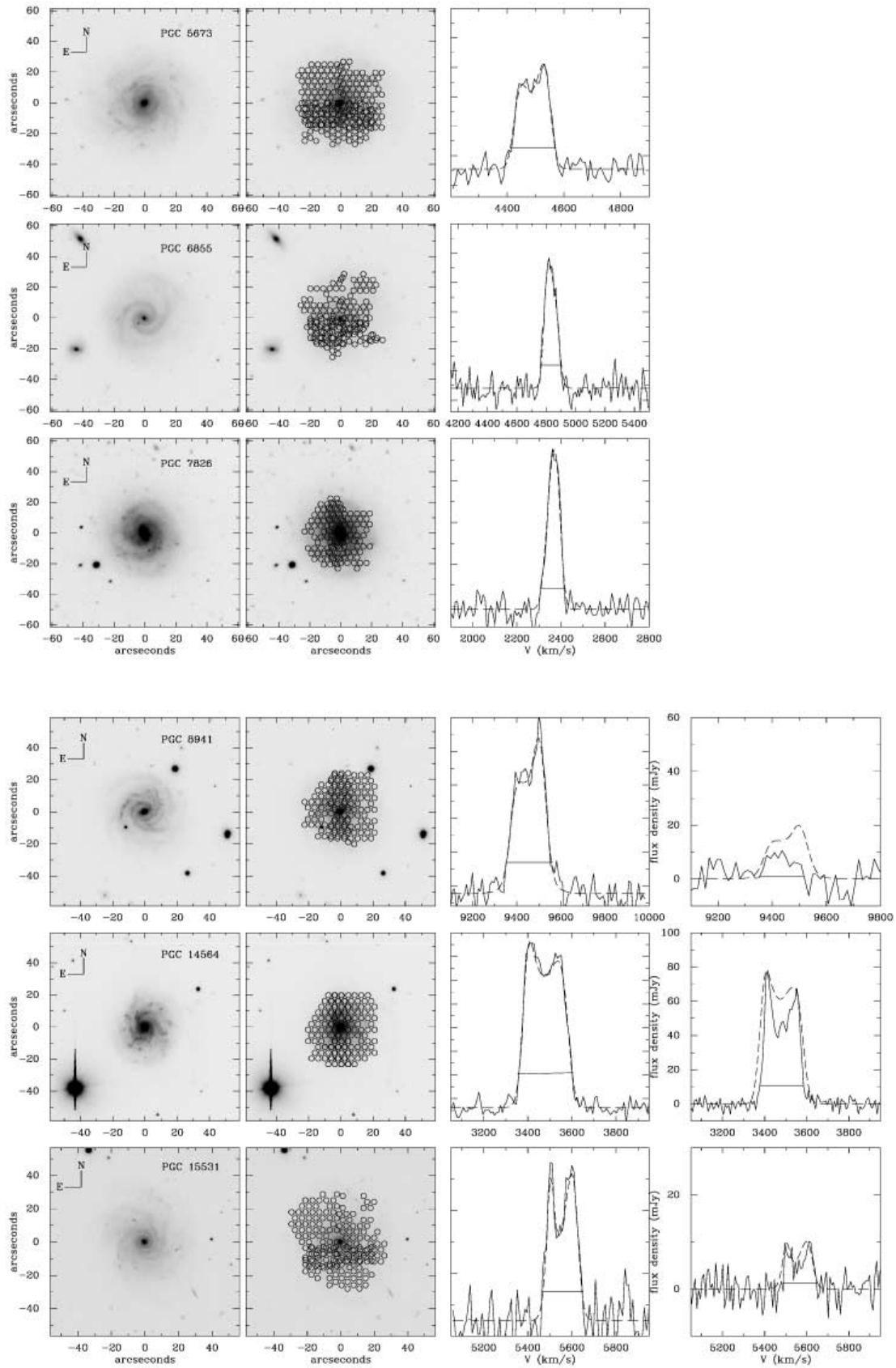
Fɪɢ. 8.—Continued

518

Fig. 8.—*Continued*

FIG. 8.—*Continued*

F<small>IG</small>. 8.—*Continued*

Fig. 8.—*Continued*

522
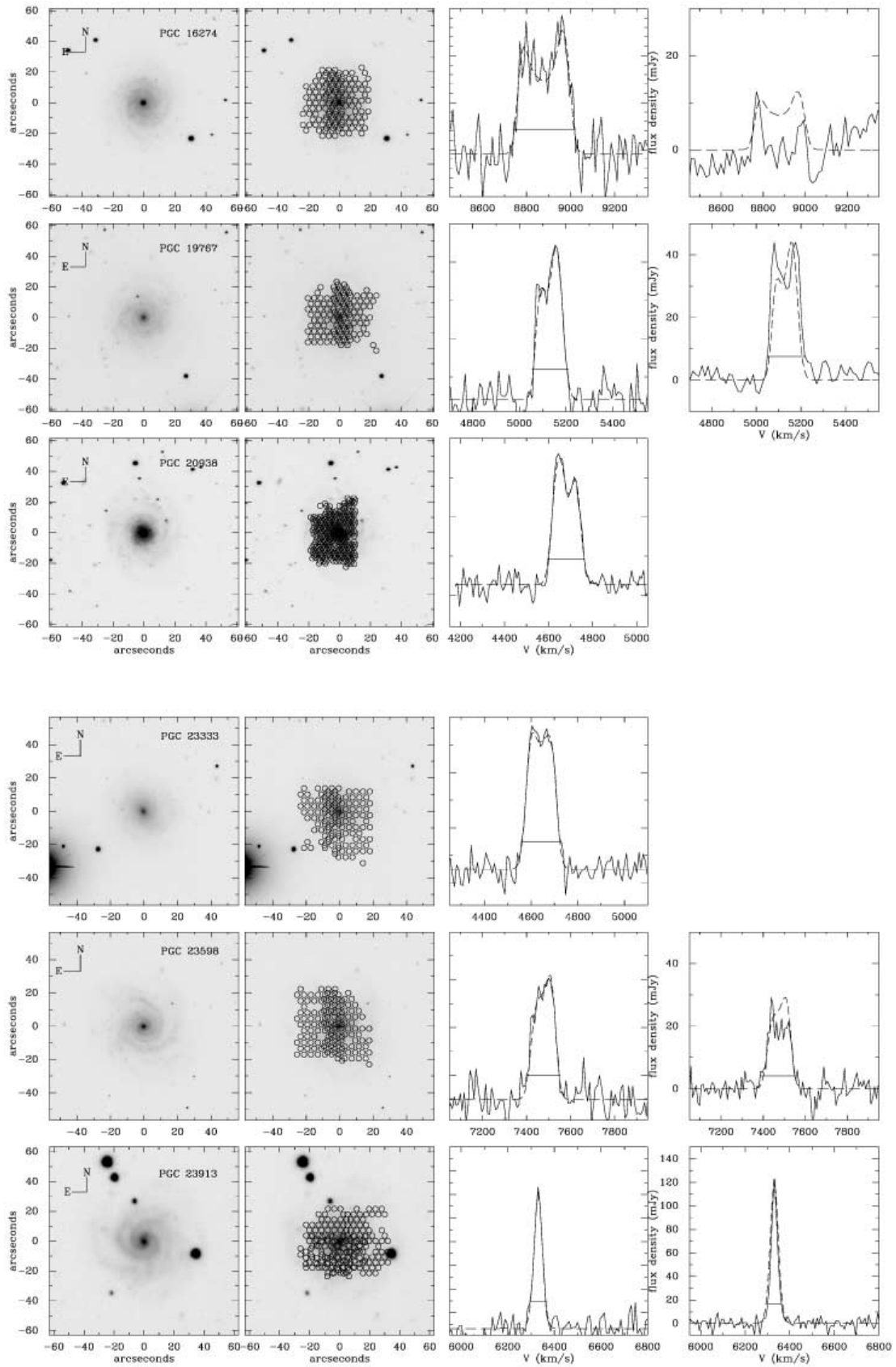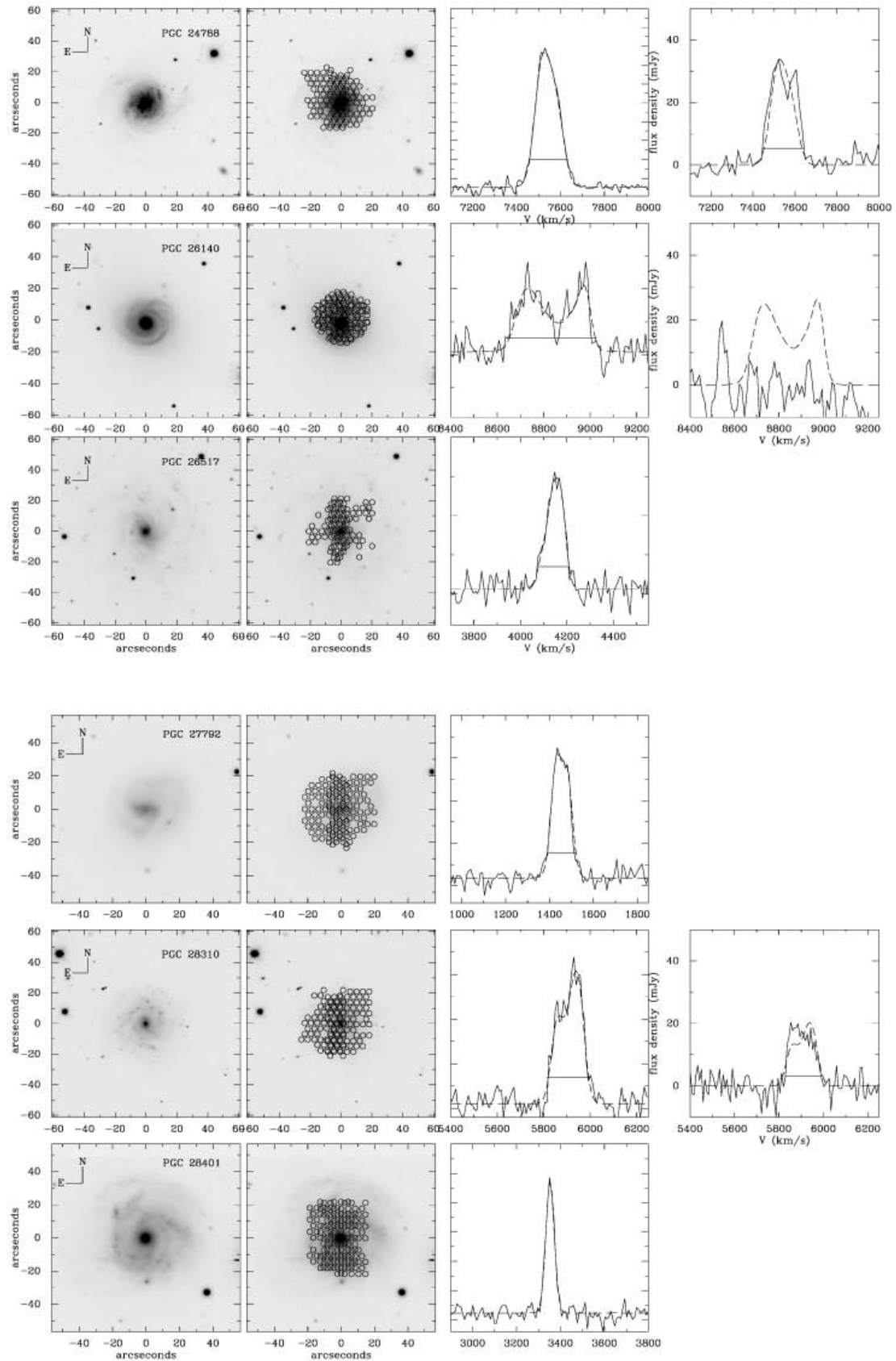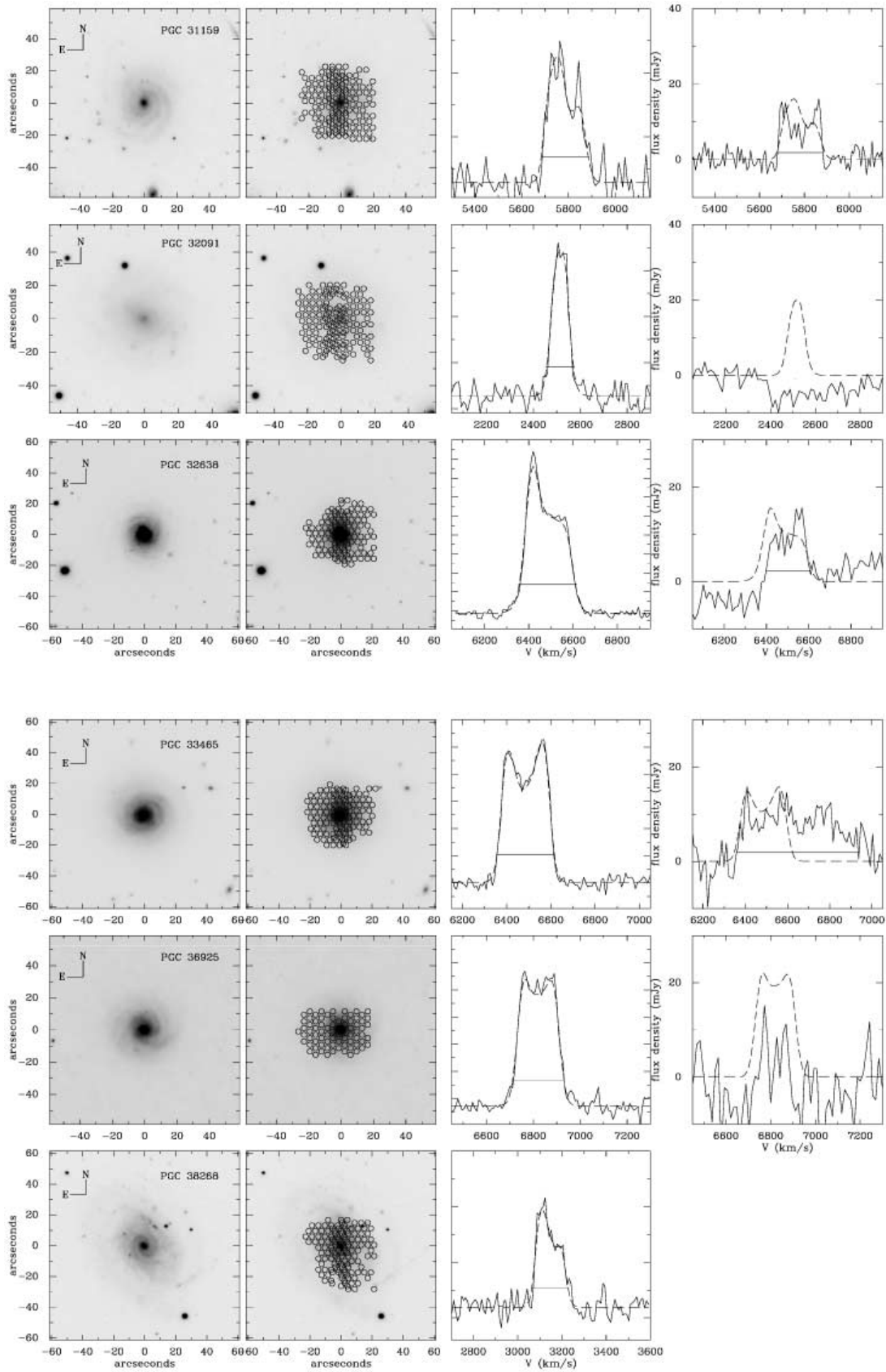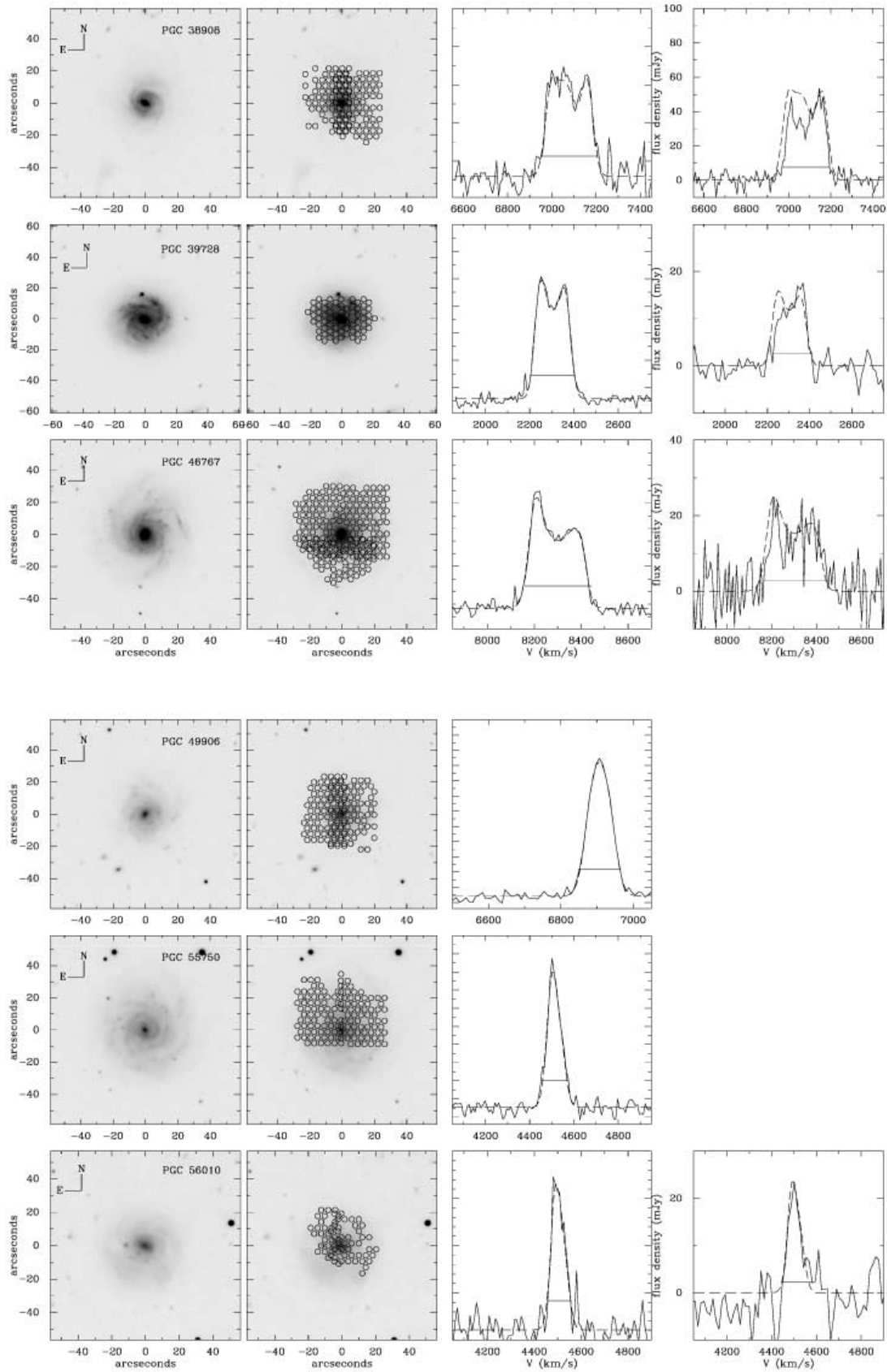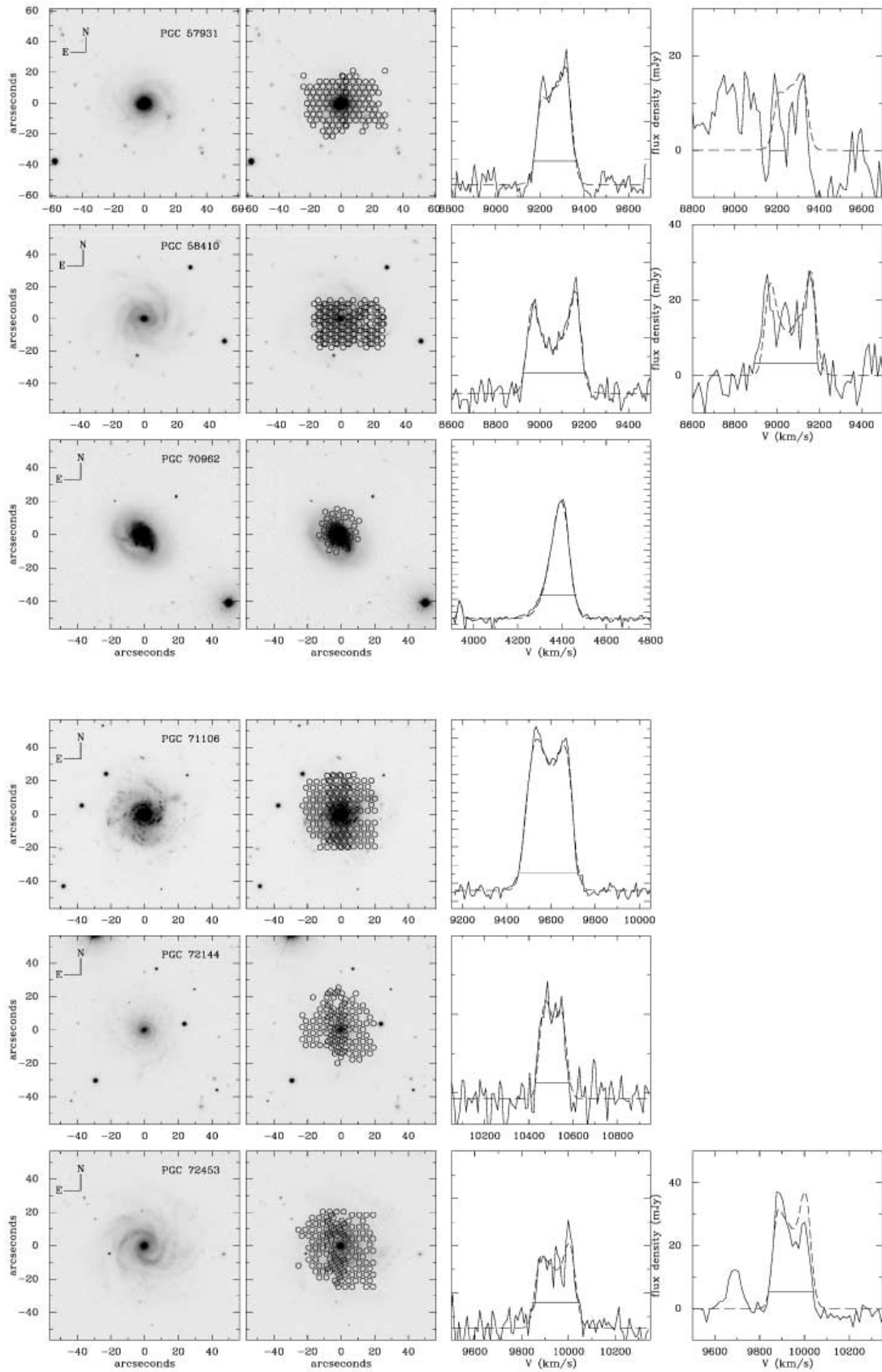
FIG. 8.—*Continued*

with redshift ($V = 8570 \pm 33$ km s^{-1}; LEDA), size, and magnitude similar to those the face-on spiral ($V = 8760 \pm 141$ km s^{-1}). Although our central H I velocity (8575 km s^{-1}) is closer to the optical velocity of the elliptical, we expected it to be gas-poor and our 21 cm line detection should not be confused by it. PGC 26140 was not detected at Arecibo (Giovanardi & Salpeter 1985) with a quoted 3 σ upper limit of 1.6 Jy km s^{-1} for a 300 km s^{-1} wide flat-topped profile, considerable lower than our detected integrated line flux of 3.1 Jy km s^{-1}. We can conclude that the H I mass for this galaxy lies far below the predicted mass, $\sim$10.3 log $M_{H I}$, based on its luminosity and type (Roberts & Haynes 1994).

PGC 28310.—Hα and H I line widths are equivalent, and both profiles are asymmetric. The detailed shapes of the profiles, however, are markedly different.

PGC 31159.—H I and Hα line profiles are equivalent, but the H I profile is double peaked, while the Hα profile is not.

PGC 32091.—No H I flux was detected.

PGC 32638.—Nançay observations have a poor baseline, making a comparison between Hα and H I line widths difficult.

PGC 33465.—Nançay observations have a poor baseline, making a comparison between Hα and H I line widths difficult.

PGC 36925.—No H I flux from the source was detected.

PGC 38908.—H I and Hα line widths are very similar. The only notable difference is the slightly broader width of the Hα profile.

PGC 39728.—H I and Hα line widths are very similar. The H I profile displays a strong asymmetry that is not observed in the Hα profile.

PGC 46767.—H I profile has a low S/N, but the Hα and H I profiles and profile-asymmetries are similar nonetheless. W_{20} measured from Nançay profile is significantly larger than one would expect from the profile due to the baseline noise.

PGC 55750.—The spatial coverage of the DensePak pointings were insufficient to cover the disk of the galaxy (Observations were performed for only 2 of 3 planned pointings).

PGC 56010.—Neither line profiles show much evidence for rotation. The spatial coverage of the DensePak pointings were insufficient to cover the disk of the galaxy (Observations were performed for only 2 of 3 planned pointings).

PGC 57931.—Nançay observations have a poor baseline, making a comparison between Hα and H I line widths difficult.

PGC 58410.—H I and Hα line profiles are very similar.

PGC 72453.—Hα and H I line widths are equivalent, and both profiles are asymmetric. The detailed shapes of the profiles, however, are markedly different.

6. SUMMARY AND DISCUSSION

We used the Principal Galaxy Catalog to choose a sample of 39 disk galaxies that span a range in luminosity, surface brightness and type. For this sample, we gathered Hα emission-line data for 39 nearly face-on spiral galaxies with the DensePak IFU on WIYN. These observations provide a fairly uniform spatial sampling of the ionized gas out to radii of approximately 3 scale lengths with a spectral resolution sufficient to yield emission-line velocities with a centroiding accuracy of $\sim$2 km s^{-1}.

For one of these galaxies, PGC 38268, we collected a deep narrowband Hα image. By comparing the DensePak data to the narrowband image, we found that the 2″8 DensePak fibers and 3 times longer exposures enabled us to detect discrete line emission over a much larger filling factor than apparent in the narrowband images. Despite the different detection thresholds, we used the PGC 38268 narrowband image convolved with a model of the velocity field obtained from the DensePak data to construct a spatially integrated, Hα line profile that accounts for all Hα gas

in the galaxy. A line profile constructed using only the DensePak data, despite not accounting for all the ionized gas, still was able to produce a comparable, integrated line width. Qualitatively, the two Hα emission-line profiles exhibited the same width *and* asymmetry. Having demonstrated that DensePak observations can be used to produce a realistic line profile for PGC 38268, we generated spatially integrated Hα line widths for all galaxies in our sample.

We have also measured the spatially resolved velocity dispersion for ionized gas in our sample. For the 6000 IFU spectra that were well fitted by a single Gaussian (and therefore less sensitive to beam smearing), we remark that under the assumption that the thermal line width for ionized gas at 10^4 K is $\sigma = 9.1$ km s^{-1} (Osterbrock 1989), and the intrinsic line width is $\sigma = 3$ km s^{-1}, then following the quadrature formalism of Jiménez-Vicente et al. (1999), the turbulent motions for H II in our sample ranges from 7.7 to 24.2 km s^{-1} (80%). This range may seem large but is in keeping with the amplitude and range seen in Fabry-Perot studies of much smaller samples of galaxies (cf. Jiménez-Vicente et al. 1999). Perhaps surprisingly, significant variations and similar amplitudes are seen in the molecular and neutral gas—albeit in small samples. For instance, Combes & Becquaert (1997) find 6 and 8.5 km s^{-1} dispersions for CO in NGC 628 and NGC 3938, respectively. While van der Kruit & Shostak (1982, 1984) have remarked on the constancy of H I velocity dispersions in disks ranging from 7 to 10 km s^{-1}, this is based on radiosynthesis observations of three galaxies. One of these galaxies, NGC 1058, was reobserved by Dickey et al. (1990) at higher spectral resolution. They found a lower H I velocity dispersion of 5.7 km s^{-1}. Both Shostak & van der Kruit (1984) and Kamphuis & Sancisi (1993) have also noted H I velocity dispersions in two late-type, nearly face-on disk decrease from 10–13 km s^{-1} in the inner disk (what Kamphuis & Sancisi call the "turbulent regions of the optical disks") to 6–8 km s^{-1} in the outer disk. While the physical mechanisms driving the velocity dispersions of the different ISM phases may indeed be different (cf. McKee & Ostriker 1977; Jog & Ostriker 1988), our primary points here is the variation of turbulent motions from galaxy to galaxy and within galaxies in all phases may be more significant than previously supposed. We will return to this issue in the context of the ionized gas in latter papers in this series.

We gathered available, spatially integrated H I line profiles from the literature and augmented them with new 21 cm observations from the Nançay radio telescope. We have presented new H I line profiles for 23 galaxies, along with measures of their line widths and H I fluxes. These data allow us to compare line profiles of ionized and neutral hydrogen. For galaxies with sufficient S/N in their H I profiles, we found excellent agreement between the width of the profiles, indicating that we are sampling the flat portion of the velocity fields in Hα for most of this sample. However, the sample of H I and Hα line profiles showed significantly different profile shapes, indicating that we are observing different distributions in the ionized versus neutral gas.

We have shown that integral field spectroscopy does an admirable job of obtaining integrated line widths. Line profiles from Nançay have S/N ratios far less than the S/N ratios for line profiles constructed from DensePak data. Yet the Nançay radio telescope has a collecting area more than 800 times greater than WIYN, and we used an average on-source integration 2 times longer per galaxy in H I than for Hα. Even if we ignore the different signal-to-noise ratios of the lines, and account for the fact that radio telescopes are roughly 100 times less expensive per m^2 than optical telescopes (of comparable steerability; van Belle et al. 2004), and that H I observations can be carried out during daylight hours,

the enhanced cost effectiveness of DensePak-to-Nançay observations is greater than a factor of 5. Since our data were taken, Nançay has undergone an extensive upgrade that has increased the sensitivity by a factor of ~5, which brings the cost effectiveness roughly to unity. High S/N H I line profile observations using the Green Bank 43 m and Arecibo 305 m radio telescopes have comparable cost effectiveness to our DensePak observations (e.g., Haynes et al. 1998, 1999). Yet the true forte of Hα integral field spectroscopy is the high spatial resolution of resolved velocity fields and the simultaneous observations of multiple atomic species. Typical radiosynthesis H I maps require 10–20 hr of integration on Westerbork or the VLA, with most radio observations using beam sizes of 15″ or greater. This is characteristically 5 times longer integrations at 5 times lower resolution than DensePak. H I and Hα observations probe different ions and physical scales, and so remain complementary. However, with the relatively recent advent of bidimensional optical spectroscopy with DensePak and related IFUs, it appears that efficient kinematic studies within the inner (optically bright) regions of galaxies are now squarely in the optical regime.

REFERENCES

Andersen, D. R., & Bershady, M. A. 2003, ApJ, 599, L79
Andersen, D. R., Bershady, M. A., Sparke, L. S., Gallagher, J. S., & Wilcots, E. M. 2001, ApJ, 551, L131
Athanassoula, E. 2004, IAU Symp. 220, Dark Matter in Galaxies, ed. S. D. Ryder, D. J. Pisano, M. A. Walker, & K. C. Freeman (San Francisco: ASP), 255
Baldwin, J. E., Lynden-Bell, D., & Sancisi, R. 1980, MNRAS, 193, 313
Barden, S. C., Sawyer, D. G., & Honeycutt, R. K. 1998, Proc. SPIE, 3355, 892
Barnes, E. I., & Sellwood, J. A. 2003, AJ, 125, 1164
Beauvais, C., & Bothun, G. 1999, ApJS, 125, 99
Bershady, M. A., Andersen, D. R., Harker, J., Ramsey, L. W., & Verheijen, M. A. 2004, PASP, 116, 565
Bershady, M. A., Andersen, D. R., Verheijen, M. A. W., Westfall, K. B., Crawford, S. M., & Swaters, R. A. 2005, ApJS, 156, 311
Bournard, F., Combes, F., Jog, C. J., & Puerari, I. 2005, A&A, 438, 507
Cardelli, J. A., Clayton, G. C., & Mathis, J. S. 1989, ApJ, 345, 245
Chemin, L., et al. 2006, MNRAS, 366, 812
Combes, F., & Becquaert, J.-F. 1997, A&A, 326, 554
Conselice, C. J., Bershady, M. A., & Jangren, A. 2000, ApJ, 529, 886
Courteau, S. 1997, AJ, 114, 2402
Courteau, S., & Rix, H. W. 1999, ApJ, 513, 561
Dale, D. A., et al. 2001, AJ, 121, 1886
Davis, M., Efstathiou, G. Frenk, C. S., & White, S. D. M. 1985, ApJ, 292, 371
de Vaucouleurs, G., de Vaucouleurs, A., Corwin, H. G., Jr., Buta, R. J., Paturel, G., & Fouque, P. 1991, Third Reference Catalogue of Bright Galaxies (Austin: Univ. Texas)
Dickey, J. M., Hanson, M. M., & Helou, G. 1990, ApJ, 352, 522
Dubinski, J. 1994, ApJ, 431, 617
Dubinski, J., & Carlberg, R. G. 1991, ApJ, 378, 496
Fouqué, P., Durand, N., Bottinelli, L., Gouguenheim, L., & Paturel, G. 1990, A&AS, 86, 473
Franx, M., & de Zeeuw, T. 1992, ApJ, 392, L47
Frenk, C. S., White, S. D. M., Davis, M., & Efstathiou, G. 1988, ApJ, 327, 507
Giovanardi, C., & Salpeter, E. E. 1985, ApJS, 58, 623
Hayashi, E., et al. 2004, ApJL, submitted (astro-ph/0408132)
Haynes, M. P., Hogg, D. E., Maddalena, R. J., Roberts, M. S., & van Zee, L. 1998, AJ, 115, 62
Haynes, M. P., et al. 1999, AJ, 117, 2039
Homeier, N., & Gallagher, J. S. III. 1999, ApJ, 522, 199
Jiménez-Vicente, J., & Battaner, E. 2000, A&A, 358, 812
Jiménez-Vicente, J., Battaner, E., Rozas, M., Castañeda, H., & Porcel, C. 1999, A&A, 342, 417
Jing, Y. P., Mo, H. J., Borner, G., & Fang, L. Z. 1995, MNRAS, 276, 417
Jing, Y. P., & Suto, Y. 2002, ApJ, 574, 538
Jog, C. J. 1999, ApJ, 522, 661
———. 2000, ApJ, 542, 216
———. 2002, A&A, 391, 471

Jog, C. J., & Ostriker, J. P. 1988, ApJ, 328, 404
Kamphuis, J., & Sancisi, R. 1993, A&A, 273, L31
Kennicutt, R. C., Edgar, B. K., & Hodge, P. W. 1989, ApJ, 337, 761
Kornreich, D. A., Haynes, M. P., & Lovelace, R. V. E. 1998, AJ, 116, 2154
Kornreich, D. A., Haynes, M. P., Lovelace, R. V. E., & van Zee, L. 2000, AJ, 120, 139
Levine, S. E., & Sparke, L. S. 1999, ApJ, 521, 798
Matthews, L. D., van Driel, W., & Gallagher, J. S. 1998, AJ, 116, 1169
Matthews, L. D., van Driel, W., & Monnier-Ragaigne, D. 2001, A&A, 365, 1
McKee, C. F., & Ostriker, J. P. 1977, ApJ, 218, 148
Navarro, J. F., Frenk, C. S., & White, S. D. 1996, ApJ, 462, 563
———. 1997, ApJ, 490, 493
Noordermeer, E., Sparke, L. S., & Levine, S. E. 2001, MNRAS, 328, 1064
Osterbrock, D. E. 1989, Astrophysics of Gaseous Nebulae and Galactic Nuclei (Mill Valley: University Science Books)
Paturel, G., et al. 1997, A&AS, 124, 109
———. 2003, A&A, 412, 57
Persic, M., Salucci, P., & Stel, F. 1996, MNRAS, 281, 27
Richter, O.-G., & Sancisi, R. 1994, A&A, 290, L9
Rix, H. W., & Zaritsky, D. 1995, ApJ, 447, 82
Roberts, M. S., & Haynes, M. P. 1994, ARA&A, 32, 115
Rozas, M., Relaño, M., Zurita, A., & Beckman, J. E. 2002, A&A, 386, 42
Rozas, M., Zurita, A., Beckman, J. E., Pérez, D. 2000, A&AS, 142, 259
Rubin, V. C., Waterman, A. H., & Kenney, J. D. P. 1999, AJ, 118, 236
Ryden, B. 2004, ApJ, 601, 214
Sawyer, D. 1997, Dense Pak Users Manual (Tucson: WIYN), http://www.noao.edu/wiyn/densepak.pdf
Schlegel, D. J., Finkbeiner, D. P., & Davis, M. 1998, ApJ, 500, 525
Schoenmakers, R. H. M. 1999, Ph.D. thesis, Rijkuniversiteit Groningen, Netherlands
Schoenmakers, R. H. M., Franx, M., & De Zeeuw, P. T. 1997, MNRAS, 292, 349
Shostak, G. S., & van der Kruit, P. C. 1984, A&A, 132, 20
Simon, J., Bolatto, A. D., Leroy, A., & Blitz, L. 2003, ApJ, 596, 957
Swaters, R. A., Schoenmakers, R. H. M., Sancisi, R., & van Albada, T. S. 1999, MNRAS, 304, 330
Swaters, R. A., Verheijen, M. A. W., Bershady, M. A., & Andersen, D. R. 2003, ApJ, 587, L19
Theureau, G., et al. 1998, A&AS, 130, 333
van Belle, G. T., Meinel, A. B., & Meinel, M. P. 2004, Proc. SPIE, 5489, 563
van den Bosch, F. C. 2000, ApJ, 530, 177
van der Kruit, P. C., & Shostak, G. S. 1982, A&A, 105, 351
———. 1984, A&A, 134, 258
Verheijen, M. A. W., & Sancisi, R. 2001, A&A, 370, 765
Willick, J. A. 1999, ApJ, 516, 47
Zaritsky, D., & Rix, H. W. 1997, ApJ, 477, 118